UCLA
UCLA Electronic Theses and Dissertations

Title
Electric field induced spin wave generation for beyond CMOS magnonic logic devices

Permalink
https://escholarship.org/uc/item/9m703469

Author
Nath, Jayshankar

Publication Date
2012

Peer reviewed|Thesis/dissertation

eScholarship.org Powered by the California Digital Library
University of California

UNIVERSITY OF CALIFORNIA

Los Angeles

Electric field induced spin wave generation for beyond CMOS magnonic logic devices

A thesis submitted in partial satisfaction
of the requirements for the degree of Master of Science
in Electrical Engineering

by

Jayshankar Nath

2012

ABSTRACT OF THE THESIS

Electric field induced spin wave generation
for beyond CMOS magnonic logic devices

by

Jayshankar Nath

Master of Science in Electrical Engineering
University of California, Los Angeles, 2012
Professor Kang L. Wang, Chair

The semiconductor industry is fast approaching the fundamental scaling limit of conventional complementary metal-oxide-semiconductor (CMOS) devices. This has spurred numerous exploratory researches in the last decade, on technologies that can sustain Moore's law and eventually replace CMOS based devices. One such magnonics based, beyond CMOS device is called the spin wave device. A spin wave device is a low power magnetic logic device that uses a propagating wave of precessional spins, called a spin wave, to perform computations. Traditionally, spin waves have been generated using energetically inefficient, inductively coupled antennas. In order to attain atto-joule energy per operation, which is substantially lower than that of the current generation of CMOS devices, we propose and demonstrate a novel method of spin wave generation using the strain mediated magneto electric effect. We have conducted extensive experimental and numerical studies to design, engineer and fabricate such nano scale spin wave devices. These devices could in effect outperform and eventually replace the CMOS based logic devices.

The thesis of Jayshankar Nath is approved

Yaroslav Tserkovnyak

Dejan Markovic

Kang L. Wang, Committee Chair

University of California, Los Angeles

2012

To my Family

Table of Contents

List of Figures

Acknowledgements

The work presented here has been possible due to the encouragement, guidance, help and support of many.

First and foremost, I would like to deeply thank my advisor, Professor Kang L. Wang for providing me with this opportunity to carry out my graduate research under his guidance. I am especially grateful for the freedom he offered to pursue my intellectual interests. I have not only enriched my knowledge, but also obtained valuable life lessons from him. His dedication to the pursuit of knowledge and his work ethics has had a profound effect on me.

I would also like to thank Professors Yaroslav Tserkovnyak and Dejan Markovic for being part of my graduate thesis committee. Their valuable insights on theoretical and circuit level aspects of this work are greatly appreciated. I am also thankful to Alex Khitun for starting this project on magnonic logic devices.

I am especially grateful to Sergiy Cherepov for his constant guidance, help and support in almost all aspects of this work. I have learned a vast amount from him, both technical and otherwise. He has played a vital role in my transition to this graduate life. I would like to express my sincere gratitude to Pedram Khalili as well. His guidance and insightful critique has been pivotal to my work. I would also like to thank Juan G. Alzate for his technical and personal guidance.

I am especially thankful to Kin L. Wong, Yen-Ting Lin and Mark Lewis for helping me with the sample fabrications. Their valuable inputs were vital in designing the nanofabrication process flow. In particular, I would like to thank Yen Ting Lin for his enormous patience and help in the e-beam lithography process. In this regard, I would like to thank Yuwei Fan as well. The e-beam lithography of our device was riddled with complications due to the non standard substrate used. Yuwei Fan spent hours in the clean room with us to ensure that we could overcome all the e-beam related problems.

I am grateful to Mingqiang Bao and Pramey Upadhyaya for help with the theoretical aspects of this work. I would like to acknowledge Professor Yaroslav Tserkovnyak's group in this regard as well. I would also like to acknowledge Professor Gregory Carman's group for help relating to magneto electric materials. I am thankful to Guodong Zhu of the Fudan University as well. I am also grateful to Tajendra Vir Singh and Edson Smith of the Institute of Digital Research and Education (IDRE), UCLA for the help with and the in-depth tour of the Hoffman 2 cluster.

My gratitude to all the members and staff of the Device Research Laboratory (DRL) at UCLA. I would also like to thank all the members of the Office of Student Affairs, Electrical Engineering, UCLA for their help. I would especially like to thank Deeona Columbia for helping me navigate through all the administrative procedures and paperwork. I would also like to thank the staff of the Electrical Engineering Department, UCLA as well as the staff of ISNC, CNSI.

My gratitude to the University of California, Los Angeles (UCLA), the Defense Advanced Research Projects Agency (DARPA) and the Western Institute of Nanoelectronics (WIN) for their support of this work.

I am grateful to all my friends at UCLA and at UCHA for all their support and encouragement. I would also like to thank all my friends around the world for all the wonderful experiences.

Last but not least, I would like to thank my family. All my accomplishments have been made possible by the unwavering love, guidance, help, support and sacrifices of my mother, father and sister. They stood by me in all my successes and failures. I would also like thank my grandparents, my brother-in-law and my niece. This thesis is dedicated to you all; for the enormous joy that you all bring to my heart.

1. Introduction

Driven by the ever increasing need for information processing, the semiconductor industry is fast approaching a juncture, when further dimensional scaling of the conventional complementary metal-oxide-semiconductor (CMOS) devices will become prohibitive from an energy perspective. This has led to numerous exploratory researches on technologies that can sustain Moore's law and eventually replace digital CMOS based devices[1]. One such exploratory device, based on the collective spin oscillation phenomena, is called the Spin Wave Device (SWD)[1,2]. An SWD is an ultra-low power magnetic logic device[2] that uses a propagating wave of precessional spins, called a spin wave, within a strip of ferromagnetic material, called the spin wave bus, to transfer and manipulate information. This implies that this "beyond CMOS" device is non charge-based[1], i.e. there is no actual charge transfer required to perform logical operations,

unlike field effect transistors (FET). The advantages of a wave based device are many. Namely, it enables high performance computing based on the characteristic frequency of the wave. In case of spin waves, the frequency is in the gigahertz[3] to the terahertz range[4], providing a very high bandwidth for information processing. Further, in this device, information can be encoded in both, the amplitude[5–7] or the phase of the spin wave[8–10]. This provides an increased information processing capability. Being based on wave phenomena, this device is also capable of parallel data processing utilizing multiple frequency channels[2]. Since a spin wave is more easily manipulated than light[11], an SWD holds certain advantages over photonic devices as well. But the primary advantage of an SWD is its ultra low power operation, resulting from the non existence of ohmic losses, from being a non charge-based device. In order to attain the required low power operations, it is of the utmost importance to have an energy-efficient spin wave generation scheme.

Most of the previously reported works have utilized techniques such as Brillouin Light Scattering (BLS)[12], inductive coupling using antenna[13–16], spin transfer torque (STT) using spin polarized currents[17–19] etc, for spin wave generation. However, these techniques are not energy-efficient. One of the low power alternatives is the generation of spin waves using the magneto electric (ME) effect. We estimate the energy required to generate spin waves using the ME effect to be 17aJ, as detailed later, on page 22. This number is four orders of magnitude less than the energy requirement of antenna based spin wave generation, estimated to be around 141fF. The spin wave generation using ME effect was proposed as early as 1973 by Wood and Austin[20]. But only recently has it seen renewed interest, stemming primarily from works on strain induced magnetization rotation, for use in magnetic memories[21–23]. Here, the work on spin wave generation and detection utilizing the Magneto Electric (ME) effect is presented.

2. An Overview of Spin Wave Science and Technology

In order to comprehend the working of magneto electric effect based spin wave devices, the underlying concepts are reviewed in this chapter.

2.1 Dynamic eigenmodes of a ferromagnet: Spin Waves

Ferromagnets are materials which exhibit spontaneous magnetic ordering. The first theory to explain this magnetic ordering in ferromagnetic materials was proposed by Pierre Weiss in 1907. His 'molecular field' theory postulated the existence of an internal molecular field, proportional to the magnetic moment per unit volume (Magnetization), to be responsible for the large magnetization in ferromagnets[24–29]. The origin of this molecular field was then explained independently by Frenkel and Heisenberg. Heisenberg proposed that, since the electron clouds associated with the neighboring magnetic atoms overlap, the electrostatic energy associated with the electrons should be dependent on their relative spins, based on the Pauli's

exclusion principle. This neighboring spin orientation dependent energy is called the exchange energy and is responsible for the ferromagnetic ordering[24–29]. The corresponding neighboring spin orientation dependent interaction, called the exchange interaction, is a strong, isotropic and short range interaction.

The concept of spin waves as the dynamic eigenmodes of a ferromagnetic medium was first introduced by Bloch in 1930. This lead to his work on the $T^{3/2}$ law for the temperature variation of the saturation magnetization[24–31]. Based on the Heisenberg model, the ground state of ferromagnetic media can be considered as an array of completely ordered spins, as shown in Fig. 2.1a. The first excited state of this medium may then be wrongly assumed to be one in which a single localized spin is reversed, as shown in Fig. 2.1b. But based on the Heisenberg model, such a localized spin reversal in an array of 19 spins, requires a high energy of $18JS^2$, where J is the exchange co-efficient and S is the spin of the electron. In case of a nickel strip with $J = 7.2 \times 10^{-12}\,\frac{\mathrm{J}}{\mathrm{m}}$ and $S = \frac{1}{2}$, this energy requirement can be calculated to be 32.4pJ/m. The energy associated with a spin reversal can be minimized in a dynamic system with exchange-coupled spins, which share the spin reversal as shown in Fig. 2.1c. Figure 2.2d also shows a schematic of this dynamic state[26]. This propagating wave of partial spin excitations is called a spin wave. And a quantum of this collective spin oscillation is called a magnon[31]. The energy required for such a state can be calculated to be equal to $4JS(1 - \cos(q \cdot a))$, where q is the wave vector and a is the inter-atomic spacing[26]. In case of a nickel strip with $a = 2.49.2 \times 10^{-12}$, excited by a loop antenna with $q = 7.85 \times 10^{6}$, this energy can be computed to be 27.5aJ/m, which is substantially lower than that of a single localized spin reversal mentioned in the previous case.

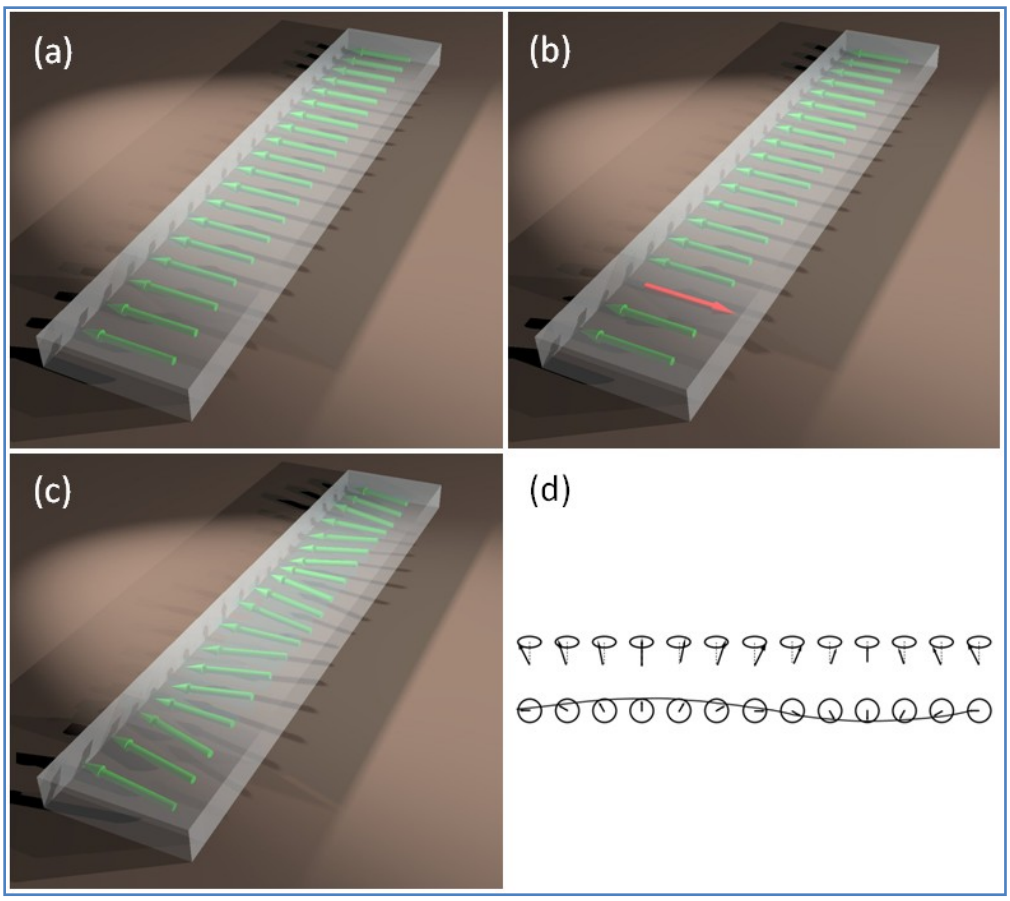

Figure 2.1: Eigen states of a ferromagnet. (a) Ground state. (b) Excited state, requiring an energy of 32.4pJ/m for the localized spin reversal. (c) Dynamic state with partial spin excitations, requiring an energy of 27.5aJ/m. (d) Schematic of a spin wave, obtained from ref. 26.

2.2 Spin Wave Device

Similar to other types of waves, interference is observed in spin waves as well. It is this linear constructive and destructive interference phenomenon, along with non linear elements in the form of non volatile ME cells to interpret the results, that is used to create logic using spin waves. When waves constructively interfere, the result can be considered as logic '1' and when the waves destructively interfere, it can be considered as logic '0' in our logic devices. A schematic of the spin wave device designed by Khitun et al. is presented in Fig. 2.2[10,32,33]. This

design consists of non volatile Magneto Electric (ME) elements, called ME cells and spin wave guides called spin wave buses. The ME cells are small magnetic islands, whose magnetization can be rotated by applying a voltage. This rotation is similar to the excitation of the ferromagnetic ground state mentioned previously. Hence, the rotation of magnetization generates spin waves in a stripe of ferromagnetic material, the spin wave bus. The generated waves propagate along the bus and undergo interference when either when two or more such buses come together or when waves generated by different ME cells reach one point along the same bus. This interference can be tailored to perform the required logic operation. The output of this logic operation can then be read out based on the rotation of the magnetization, caused by the resultant spin wave, at the output ME cell. Further, these ME cells can be designed as bi-stable magnetic elements in which the magnetization is controlled by voltage[21]. Hence the ME cells can also be used as non volatile input and output memory elements of the design. The basic spin wave device mentioned here can be utilized as a building block to create complicated logic circuits such as binary adders etc.

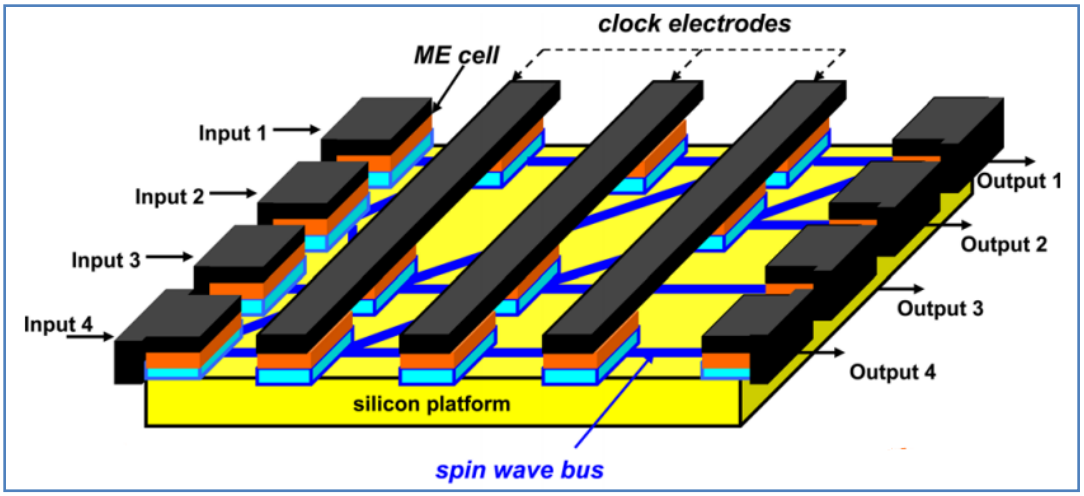

Figure 2.2: Schematic of a Spin Wave Device, obtained from ref. 33. The design consists of non volatile magneto-electric elements, for spin wave generation and detection, and spin wave bus, for guiding the spin waves.

2.3 Magneto Electric Effect

The traditional spin wave generation technique using antennas[13–16] is energetically inefficient due to ohmic losses. In order to generate spin waves in a highly energy-efficient manner, we use the ME effect. The ME effect can be defined as the manipulation of magnetization by an electric field and vice versa[20]. Van Suchtelen et al and van den Boomgaard et al.[34] were the first to implement ferroelectric- ferromagnetic (multiferroic) composite materials which exhibited the ME effect. In these ME materials, the applied electric field would induce an electric polarization, which would strain the ferroelectric phase due to the inverse piezoelectric effect. This strain, in turn would induce a change in magnetization of the ferromagnetic phase via the inverse magnetostrictive effect (also known as the Villari effect[26]). Hence, the ME effect can be considered as the product of the piezo-magnetic and the piezoelectric effects[35], as presented in Fig. 2.3[36].

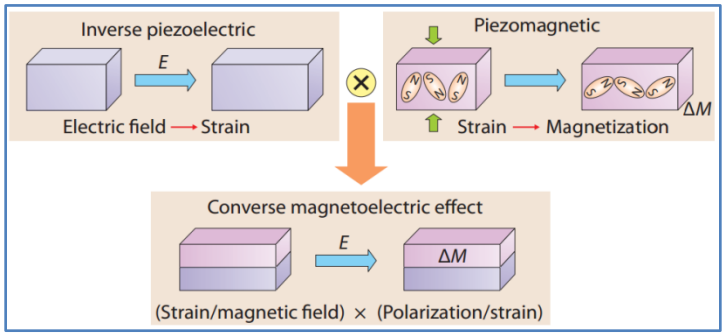

Figure 2.3: Illustration of the inverse magneto electric effect in a composite system, obtained from ref. 36.

Starting in the early 2000s, there has been a huge interest in single phase ME materials. These ME materials are part of a broad class of materials called multiferroics[37,38]. Multiferroic materials exhibit both the ferroelectric and the ferromagnetic properties. Unfortunately there are only a few room temperature multiferroic materials in which these properties are coupled and are

essentially ME[38]. Hence, in this work we use a two phase system in which the ferroelectric and the ferromagnetic phases are coupled via strain.

Wood and Austin were the first to propose the generation of spin waves using the ME effect in 1973[20]. The earliest theoretical framework for the generation of spin waves by the oscillations of the ferroelectric domain walls was developed by Chupis and Manzhos[39,40]. In 2001, Bichurin et al. proposed a theory for the ME effect in piezoelectric- magnetostrictive multilayer composites at microwave frequencies[41]. The first observation of microwave ME interactions in single crystal ferromagnetic- piezoelectric bi-layers was made by Shastry et al in 2004[42]. They performed ferromagnetic resonance studies on yittrium iron garnet (YIG; ferromagnetic) and lead magnesium niobate- lead titanate (PMN-PT; piezoelectric) bilayers.

The design proposed by Khitun et al., shown in Fig. 2.2 has ME cells consisting of a magnetostrictive and a piezoelectric layer patterned on a silicon substrate. But such a structure is quite complex to fabricate. This is primarily due to the difficulty in fabricating islands of piezoelectric material on top of the ferromagnetic layers. Hence in this work, we propose a different design which is based on a piezoelectric substrate itself. The layered structure of the device is shown in Fig. 2.4, which consists of a magnetostrictive nickel (Ni) layer and a ferromagnetic nickel-iron (NiFe) layer on a piezoelectric PMN-PT

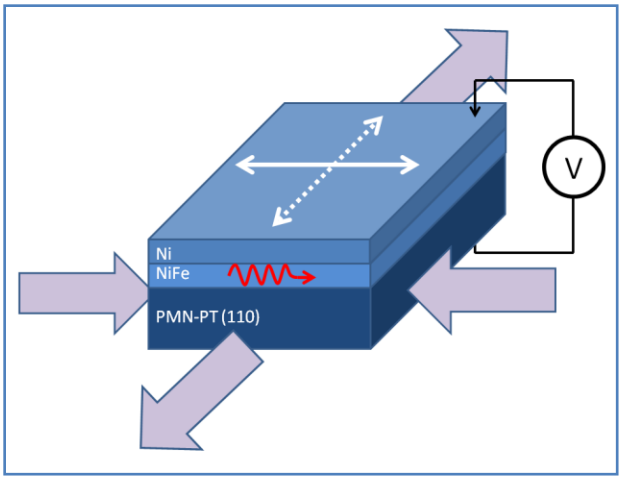

Figure 2.4: Ni/NiFe on a PMN-PT substrate. By applying a voltage across the device, a strain is induced in the PMN-PT substrate. The strain rotates the magnetization in the Ni layer, which in turn generates spin waves. These waves then propagate in the Ni/NiFe bi- layer.

substrate. When a voltage is applied across the sample, a strain is generated by the PMN-PT substrate. This strain in turn rotates the magnetization in the Ni layer and generates spin waves in the Ni/NiFe bi-layer.

Figure 2.5 shows data from Magneto Optical Kerr Effect (MOKE) measurements. In MOKE experiments, a polarized light is shone on the test material. Based on the photon-magnon interactions, the polarization of the laser beam can change due to the Kerr effect. Hence, by measuring the change in polarization of the reflected laser beam, we can determine the change in the magnetization. In this experiment, a polarized laser was shone on a Ni/NiFe bi-layer deposited on a PMN-PT substrate. With only a low voltage applied across the substrate, the data shows a high coercive field, characteristic of a magnetic easy axis. As the voltage is increased to 200V, the coercive field decreases substantially, indicating the presence of a magnetic hard axis. This experiment hence proves that by applying a voltage, we can modulate the magnetization configuration in Ni/NiFe bi-layer films.

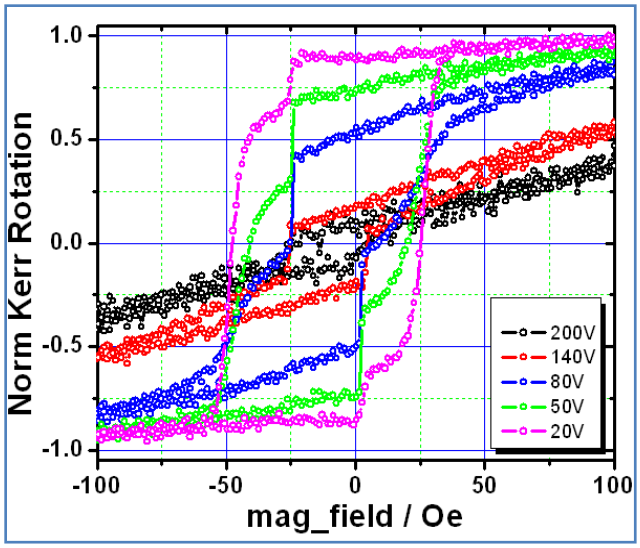

Figure 2.5: MOKE data of the Ni/NiFe/PMN-PT system. By applying a voltage across the system, the easy axis can be rotated, leading to a hard axis along the measured direction. Data used with permission from Dr. Zhu.

3. Spin Wave Generation using the Magneto Electric Effect

We conducted experimental studies on spin wave generation using magneto electric effect. The results from these experiments, presented in this chapter, are then explained based on theoretical and numerical studies. This chapter also details work on energy estimations of these devices.

3.1 RF characterization of ME cell based spin wave devices

In order to demonstrate the proof of concept, we fabricated and characterized micrometer-scale devices which used ME effect for spin wave generation and detection[43]. Figure 3.1a, b shows the high frequency probe station setup used to characterize these devices. It primarily consists of a 3D magnetic field source and a Hewlett Packard 8722ES Vector Network Analyzer (VNA) to perform magnetic field and frequency sweeps respectively.

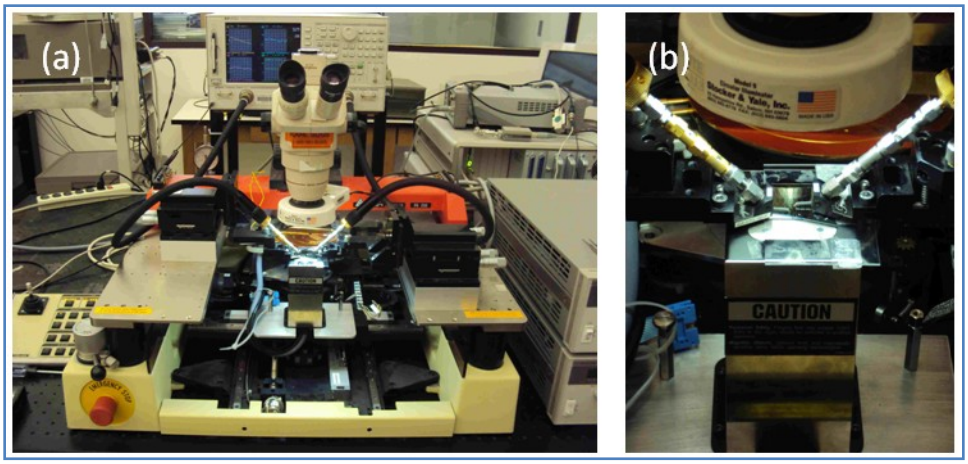

Figure 3.1: High frequency setup. (a) RF probe station with the VNA. (b) 3D magnetic field source.

The schematic of the measurement setup is shown in Fig. 3.2a and the optical micrograph of the device is shown in Fig. 3.2b. The micro-fabricated sample consists of a Ni/NiFe stripe patterned on a PMN-PT substrate, which serves as the spin wave bus. In order to excite spin waves, we use spatially periodic electrodes on the surface of the piezoelectric, called inter-digital transducers (IDT)[44,45]. IDTs have been shown to directly couple to the piezoelectric generating surface acoustic waves (SAW)[44,46]. SAWs are longitudinal compression- decompression elastic waves traveling along the surface of an elastic medium[47]. By applying a radio frequency (RF) signal to the coplanar waveguides (CPW) connected to the IDT, we can generate SAWs. Once the SAWs are generated using an RF signal, it propagates out from the IDT, straining the substrate along its path. Once it reaches the ferromagnetic bus, it generates a stress on the stripe. This stress induces anisotropy change in the magnetostrictive material and in turn generates spin waves in the spin wave bus.

The device has 100nm thick aluminum/titanium CPWs and IDTs. The IDT along with the spin wave bus constitute the ME cells. The CPWs are isolated from the substrate using a 200nm

thick SiO_2 layer. By applying an RF input to port 1 connected to input ME cell, we can excite spin waves which propagate in the ferromagnetic bus. These waves are then picked up by the output ME cell and hence the VNA at port 2. When we apply an RF input to an ME cell, part of the signal is reflected back due to impedance mismatch and a part is transmitted via spin wave propagation, as shown in the Fig. 3.2a. The device can hence, be characterized by measuring the Scattering (S-) parameters as a function of the magnetic field.

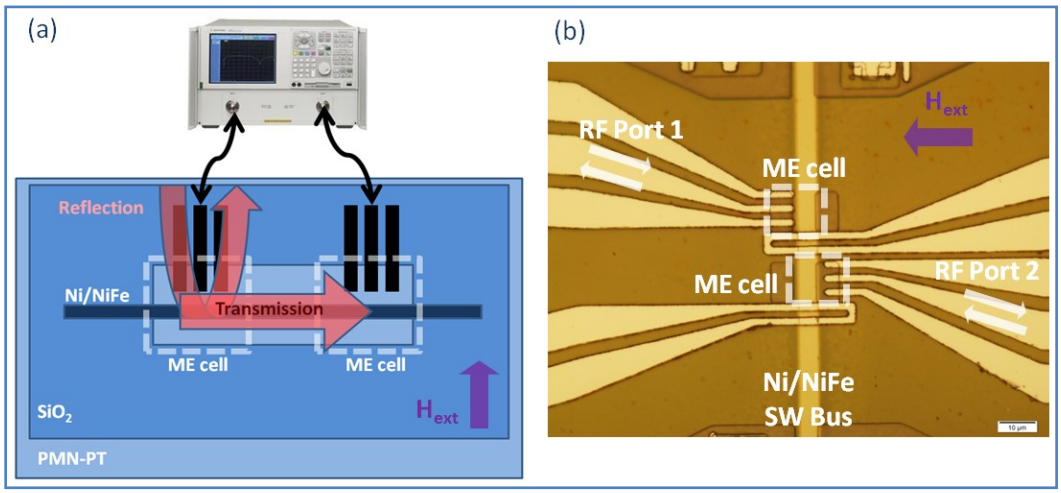

Figure 3.2: (a) Schematic of the RF measurement setup. The S-parameters are determined by measuring the reflected and the transmitted signals using a VNA. An external in-plane magnetic field is also applied to determine the magnetic field dependence of the device. (b) Optical micrograph of the device. The ME cells have been marked in the image. The device also has two antennas for reference measurements.

The results of the high frequency measurements on this micron-scale device are shown in Fig.3.3[43]. We performed frequency sweeps on the device from 10MHz to 5GHz, while sweeping the external in-plane magnetic field from -500Oe to 500Oe. By measuring the transmitted and the reflected power, we can obtain the scattering (S-) parameters. S11 and S22 represent the reflected power at the ME cells 1 and 2 respectively. The figure shows that the resonance frequency has a square root dependence on the magnetic field. This type of behavior is consistent with ferromagnetic resonance and proves that spin waves are generated by the RF input. S12 and

S21 represent the transmitted power via spin wave propagation. These plots too, show a dependence on the magnetic field. This is consistent with the fact that the generated spin waves have propagated within the spin wave bus and have been picked up at the output ME cell. Also, these signals are weaker due to spin wave damping caused by the bus. In order to de-embed the effects of magnetic field-independent electromagnetic coupling from these graphs, the frequency sweep at a high magnetic field, 1500Oe, is subtracted from the entire plot. This removes the magnetic field-independent features from the graph, de-embedding the electromagnetic coupling. To better understand these results, we have to look into the underlying theory.

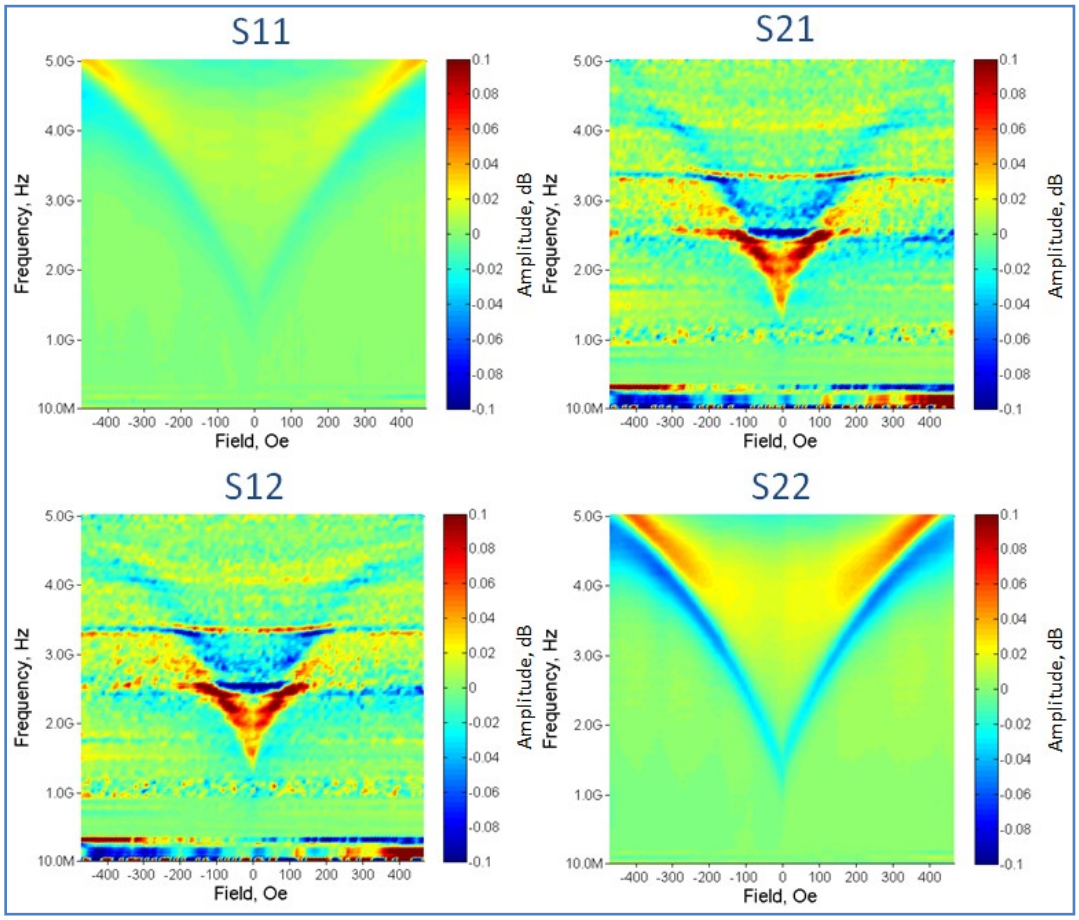

Figure 3.3: S-parameters of the device shown in Fig. 3.2b. The colors indicate the amplitude of the S-parameter. The magnetic field dependence of the device indicates the generation and propagation of spin waves. Figure obtained from ref. 43.

3.2 Theoretical basis of spin wave generation using ME effect

In order to describe magnetization dynamics, a phenomenological equation of magnetization in ferromagnets was developed by Landau and Lifshitz[25,48]. Taking into account the large internal damping in thin ferromagnetic sheets, Gilbert modified this equation of motion, in 1955[48]. The use of Landau-Lifshitz equation with the Gilbert damping term leads to the Landau-Lifshitz-Gilbert (LLG) equation as given below[49]:

$$(1+\alpha^2)\frac{d\boldsymbol{M}(t)}{d(t)} = -\gamma_0[\boldsymbol{M}(t)\times\boldsymbol{H}(t)] - \frac{\alpha\gamma_0}{M_s}\{\boldsymbol{M}(t)\times[\boldsymbol{M}(t)\times\boldsymbol{H}(t)]\} \qquad (3.1)$$

The first term on the right represents the torque exerted by the effective magnetic field **H** on the magnetic moment **M** of an electron. Since the length of the magnetization vector is conserved in the undamped case, this term describes the precession of magnetization around the effective field as shown in Fig. 3.4a[49]. The second term on the right is a damping term, which represents the dissipation caused by a field proportional to the rate of change of the magnetic moment **M**, acting on **M**. This term causes the magnetization vector to align itself with the effective magnetic field, as shown in Fig. 3.4b [49]. In this equation, α is the phenomenological Gilbert damping coefficient, M_s is the saturation magnetization and γ_0 is the gyro-magnetic ratio for an electron spin. In this equation, **H** is the vectorial sum of the externally applied magnetic field; the

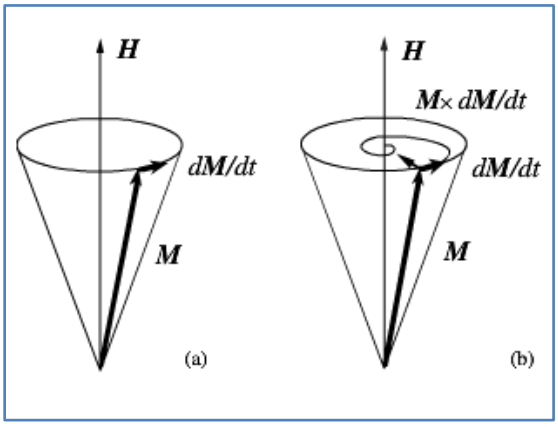

Figure 3.4: Vectorial representation of the LLG equation. (a) Undamped case. (b) Damped case. Illustration obtained from ref. 49.

demagnetization field, which results from the long range dipole-dipole interaction between the magnetic moments; the exchange field; and the anisotropy field, which results from the spin-orbital interaction. This LLG equation is commonly used to perform numerical micromagnetic studies.

In order to model the spin wave generation using ME effect, it is necessary to study the underlying physical phenomena that leads to the deflection of magnetization. In a SWD, a voltage applied to the ME cell generates a strain in the piezoelectric element. This results in a uniaxial stress, which creates a stress induced energy minimum along some fixed direction in the magnetostrictive layer. This is known as stress induced anisotropy and the ferromagnetic axis or the easy-axis is said to be directed along this fixed direction. This stress induced anisotropy and the crystalline anisotropy have the same mathematical form. Hence, in our numerical models, we use the uniaxial crystalline anisotropy to model the spin wave generation using ME effect. The uniaxial anisotropy energy density can be approximated as[26,50]:

$$E_a = K_u \sin^2 \theta \qquad (3.2)$$

Here θ is the angle between $\boldsymbol{M}$ and the anisotropy axis. Hence, the magnetization generally tends to lie along the easy axis in order to minimize the anisotropy energy. K_u gives the magnitude of the stress induced anisotropy based on the uniaxial stress σ and the saturation magnetostriction λ_s:

$$K_u = \frac{3}{2}\sigma\lambda_s \qquad (3.3)$$

Plugging eqn. (3.3) into (3.2), it is quite clear that based on the sign of λ_s the magnetization can be either parallel or perpendicular to the direction of the applied stress in order to minimize the energy. Hence, by appropriately selecting the material parameters, the induced anisotropy can lead to a rotation of the easy axis and in turn, the magnetization through the LLG equation. This can be illustrated by rewriting the eqn. (3.2) as:

$$E_a = K_u\,(1 - \cos^2\theta\,) \tag{3.4}$$

Assuming perpendicular magnetization, eqn. (3.4) can be rewritten as:

$$E_a = K_u(1 - {m_z}^2) \tag{3.5}$$

where m_z is the perpendicular component of magnetization. Using eqn. (3.5), we can determine the anisotropy field, H_a, given by:

$$H_a = -\left(\frac{dE_a}{dm_z}\right) = \frac{2K_u m_z}{M_s} \tag{3.6}$$

where M_s is the saturation magnetization, and is used to normalize the equation. H_a is a component of the effective field **H**, and hence can be substituted into eqn. (3.1) to determine the rotation of the magnetization. This change in direction of the magnetization leads to oscillations in the orientation of spins and hence, generates spin waves in the spin wave bus. With K_u dependent upon the applied voltage, eqns. (3.1) and (3.6) provide a relationship between the input voltage and the generated spin waves, which is used in the numerical modeling.

3.3 Numerical study of spin wave devices

The dynamic, spatially non uniform solutions of the LLG equation define the spin wave modes in a system. We used the Object Oriented MicroMagnetic Framework (OOMMF)[51] for our numerical studies. OOMMF utilizes the Finite Difference Time Domain (FDTD) method to solve the LLG equation. In this method, the volume of the sample is discretized, as shown in Fig. 3.5. The LLG equation is then solved in each discrete cell with the appropriate boundary conditions.

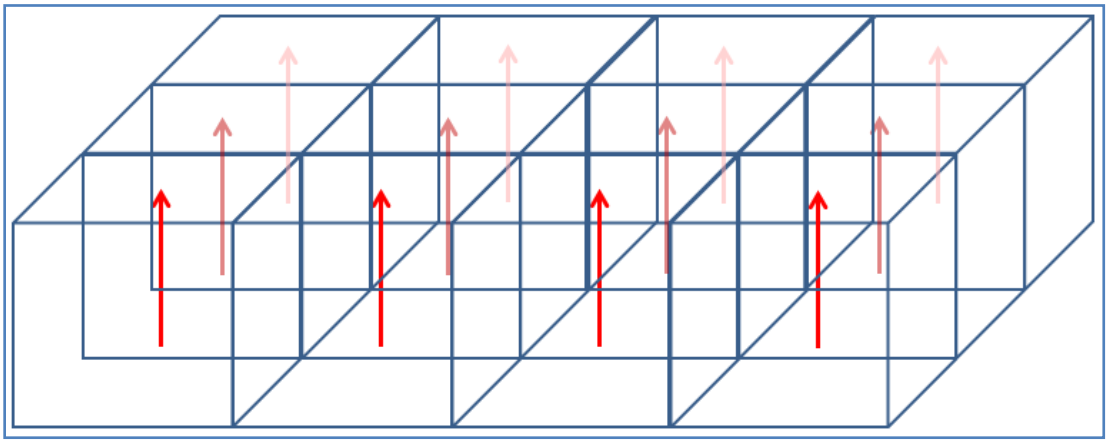

Figure 3.5: An illustration of sample discretization used for numerical studies. The LLG equation is solved in each cell using appropriate boundary conditions. The arrows indicate the initial magnetization in each cell, which can be either in-plane or out-of-plane, as shown in the figure.

In order to perform numerical studies into the spin wave generation by magneto electric effect, we developed a model shown in Fig. 3.6a. The model consists of a ferromagnetic strip, with designated inputs and outputs. The spin wave generation in the bus can be modeled using the uniaxial anisotropy rotation at the input. Once the waves are generated, they propagate along the bus and are detected at the output cell. This is accomplished by determining the rotation of magnetization at the output. These numerical studies were run on the University of California, Los Angeles (UCLA) Hoffman 2 cluster, part of which is shown in Fig 3.6b.

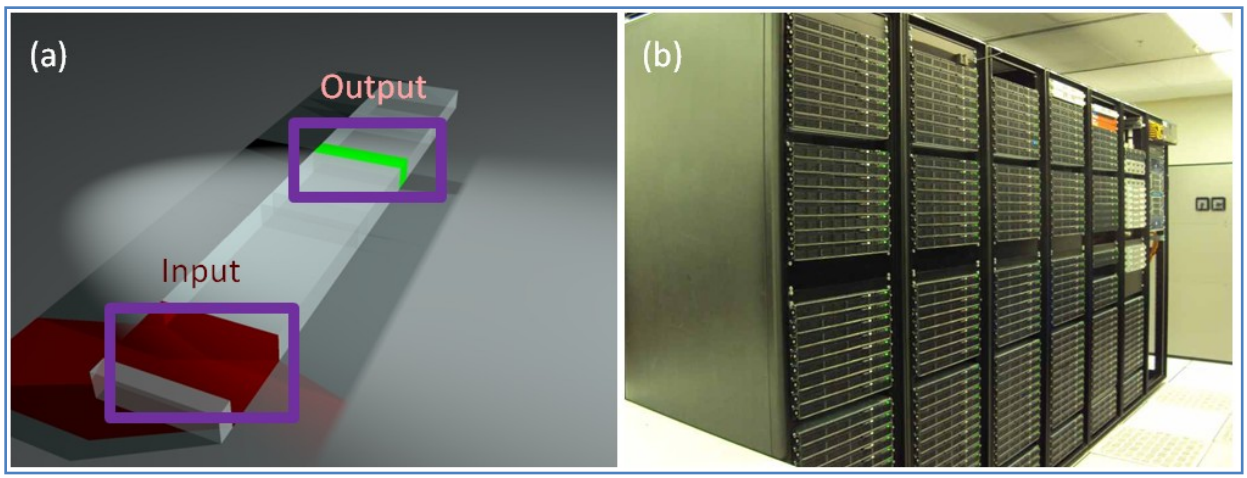

Figure 3.6: (a) Device model used in micromagnetic studies. It consists of a strip with a designated input, where the uniaxial anisotropy is rotated to generate spin waves, and an output where the spin waves can be detected based on the magnetization dynamics. (b) UCLA Hoffman 2 cluster.

Numerical studies on spin waves in a nanoscale Ni/NiFe bi-layer device, shown in Fig. 3.7, were performed. The device model consists of a 200nm wide stripe of exchange coupled Ni and NiFe layers. Each layer has a thickness of 20nm. A 2000 Oe bias field is applied along the hard axis of the magnet to saturate the magnetization as shown in Fig. 3.7b. The system is then excited by applying a 100ps square uniaxial anisotropy pulse of strength K1 = 10kJ/m^3 at the input, in the Ni layer, along the easy axis. This simulates the magnetoelastic anisotropy rotation by the magnetoelectric effect. The angle of rotation of the magnetization at the input and the outputs are then recorded.

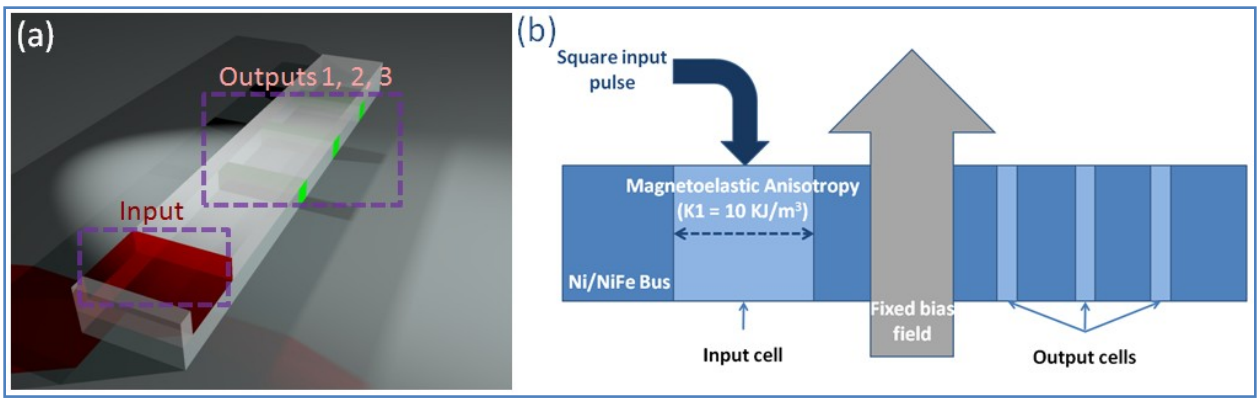

Figure 3.7: (a) Ni/NiFe bi-layer device model used for numerical studies. Each layer is 200nm in width and 20nm in thickness. (b) Schematic of the device operation. The device contains an input in the Ni layer where the uniaxial anisotropy is rotated to generate spin waves. These exchange coupled waves then propagate in the bi-layer and is picked up at the three output slices, spaced at 500nm distances, in the NiFe layer. The output slices measure the deflection of magnetization, indicative of spin wave generation and propagation.

Figure 3.8 shows the deflection of magnetization at the input and the outputs. The plots indicate a propagating spin wave packet, as marked in the figures. Figure 3.8a shows the deflection of magnetization at the input. The system is initially relaxed and then a 100ps square uniaxial anisotropy pulse is applied along the easy axis of the bus. This variation in anisotropy excites the system, leading to deflections in the magnetization, indicating spin waves. These waves then propagate down the bus and are recorded at the three outputs in the NiFe layer. The propagating, linear spin waves at the outputs are indicated in Figs. 3.8 b, c, d. From these graphs it is evident that the amplitude of the waves decreases with distance. This spin wave decay is shown in Fig. 3.9.

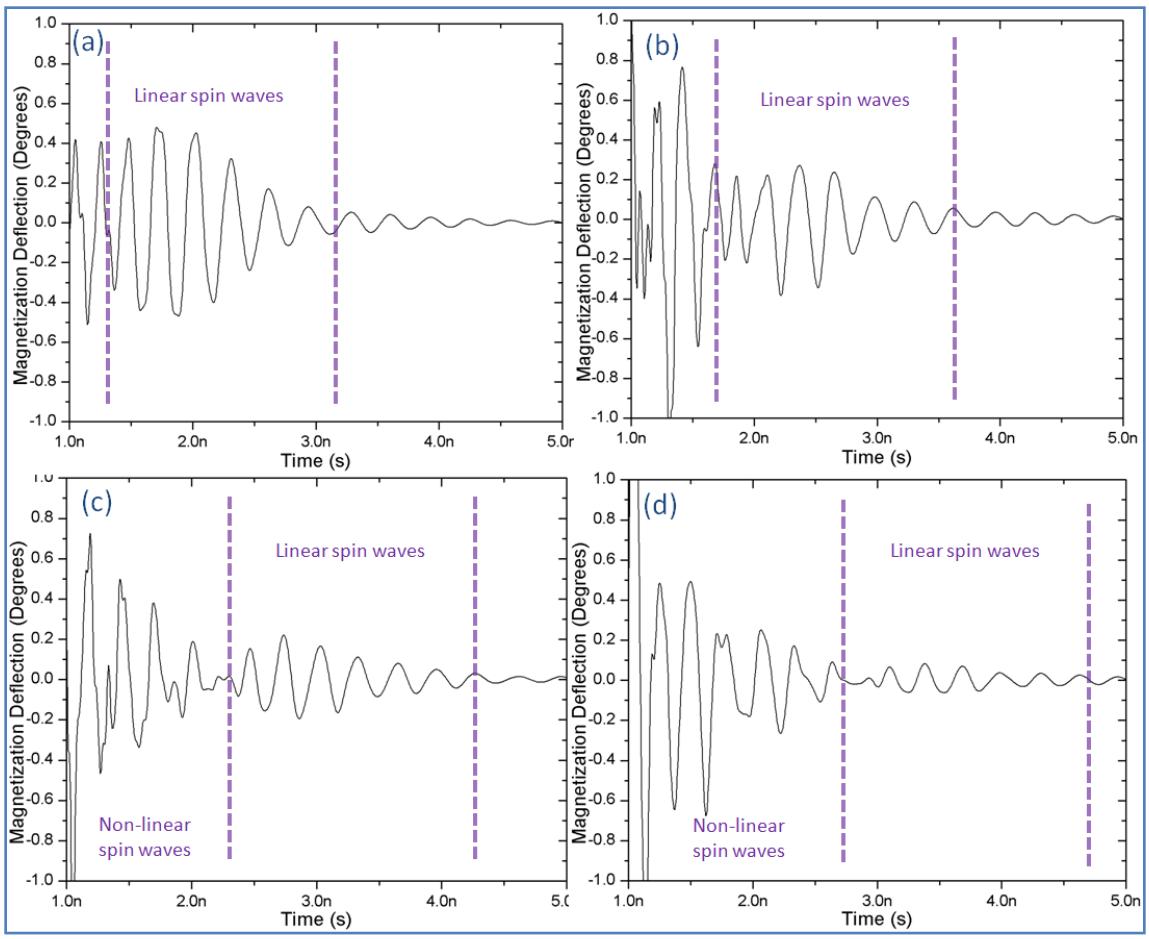

Figure 3.8: Plots representing the spin wave generation by magneto electric effect. The lines indicate the deflection of the magnetization vector in degrees. The region of linear spin waves is indicated as well. Graphs are plotted at the (a) input Ni layer (b) NiFe layer at a distance of 500nm (c) NiFe layer at a distance of 1000nm (d) NiFe layer at a distance of 1500nm.

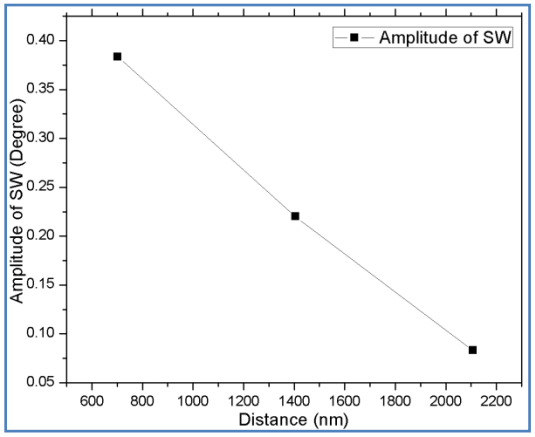

Figure 3.9: Spin wave decay in the nano device model, based on the plots of Fig. 3.8.

3.4 Experimental study on spin wave decay

In order to validate the numerical results of spin wave propagation and decay, we conducted spin wave decay measurements on a 4µm wide NiFe stripe with Ground-Signal-Ground (GSG) antennas for spin wave excitation and detection, shown in Fig. 3.10. The measurements were performed on three different devices with antenna separations of 28µm, 56µm and 84µm. The S11 plots for these devices are shown in Fig. 3.11. The magnetic field dependence is indicative of spin wave generation at the input.

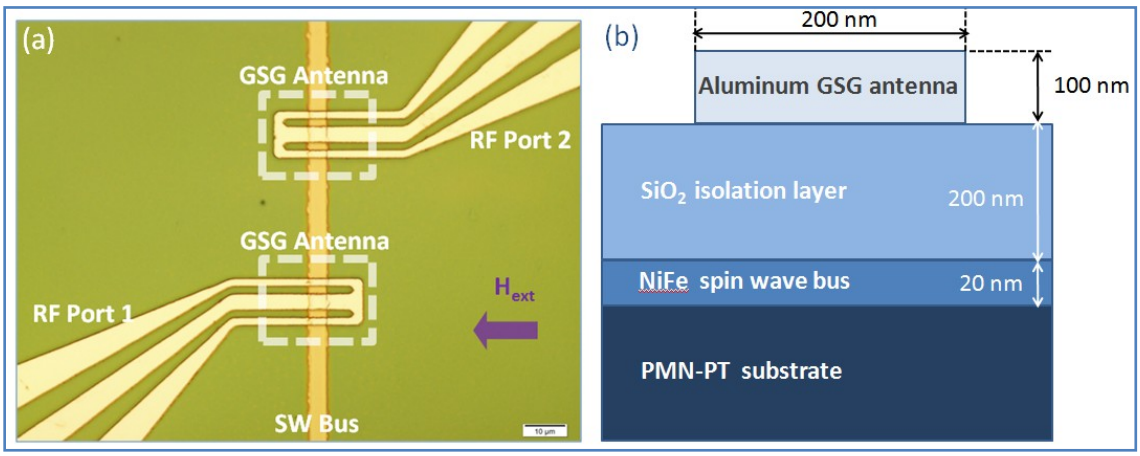

Figure 3.10: (a) Optical micrograph and (b) the cross sectional schematic of the device used for the spin wave decay measurements. The device consists of a NiFe stripe patterned on a silicon substrate. The spin waves are generated and detected using aluminum/titanium GSG antennas.

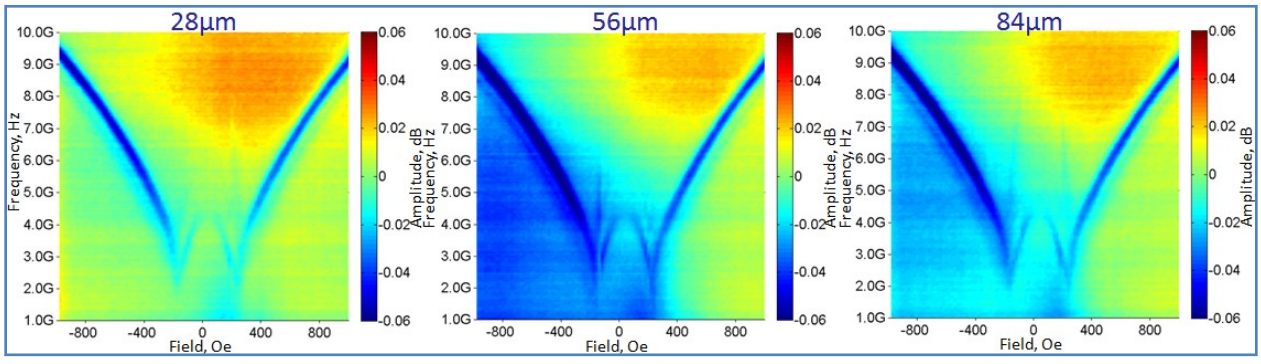

Figure 3.11: S11 amplitude plots of devices with antenna separation of 28µm, 56 µm and 84µm. The colors indicate the S11 amplitude. Ferromagnetic resonance is clearly visible in each case.

The transmitted signal, S21 plots are shown in Fig. 3.12. The square root dependence of the power on the magnetic field is indicative of spin waves. This implies that the waves generated at port 1, propagated in the ferromagnetic bus and have been detected at the port 2. Further, from the strength of the signal, it is clearly visible that the spin wave decays with increasing distance between the antennas.

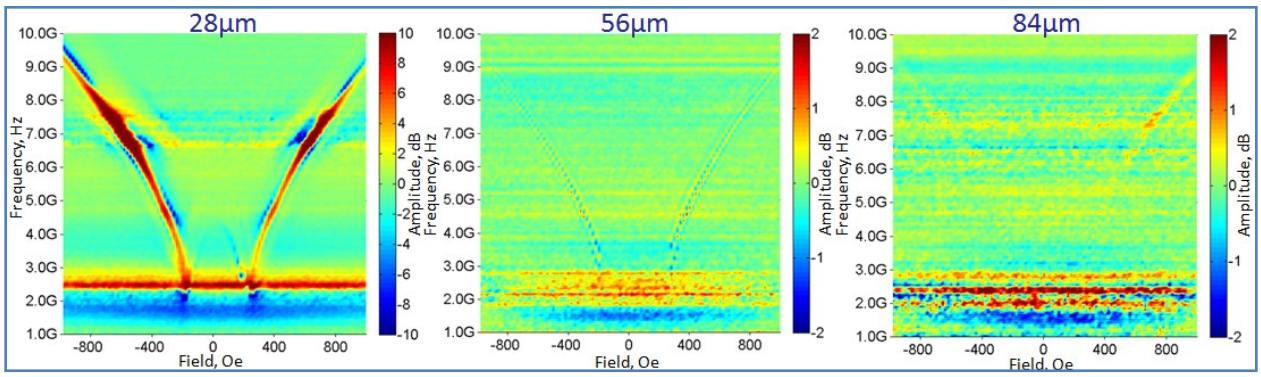

Figure 3.12: S21 amplitude plots of devices with antenna separation of 28µm, 56 µm and 84µm. The colors indicate the S21 amplitude. The spin wave decay with distance is clearly visible from the strength of the signal.

To study the spin wave decay further, we took a vertical cross section from this graph at 400Oe and re-plotted it in Fig. 3.13a. This gives us the frequency sweep at a fixed magnetic field. The different line colors are indicative of different antenna separations. The frequency at which the inductive coupling between the antenna and the spin wave bus is maximized, called the characteristic frequency of the device, is around 5GHz at 400Oe. It is indicated by the peak in the graph at this frequency. By taking a vertical cross section from this graph at 5GHz, we can obtain the spin wave decay curve, as shown in Fig. 3.13b. By curve fitting, it is evident that the spin wave decay is exponential in nature, which is consistent with similar studies. The numerical output shown previously in Fig. 3.9 does not indicate an exponential decay. Unlike Fig. 3.13b, in which the graph is based on the transmitted power, in Fig. 3.9, the spin wave decay was plotted

based on the deflection of magnetization. The decay is still expected to follow an exponential curve, based on experimental results. Also, the outputs being very close, at nanometer distances, could be another reason for not observing the exponential decay. Similar to the numerical models, we are primarily interested in nanometer scale devices, in order to improve the energy efficiency of spin wave generation. The energy metrics of the spin wave devices are detailed in the next section.

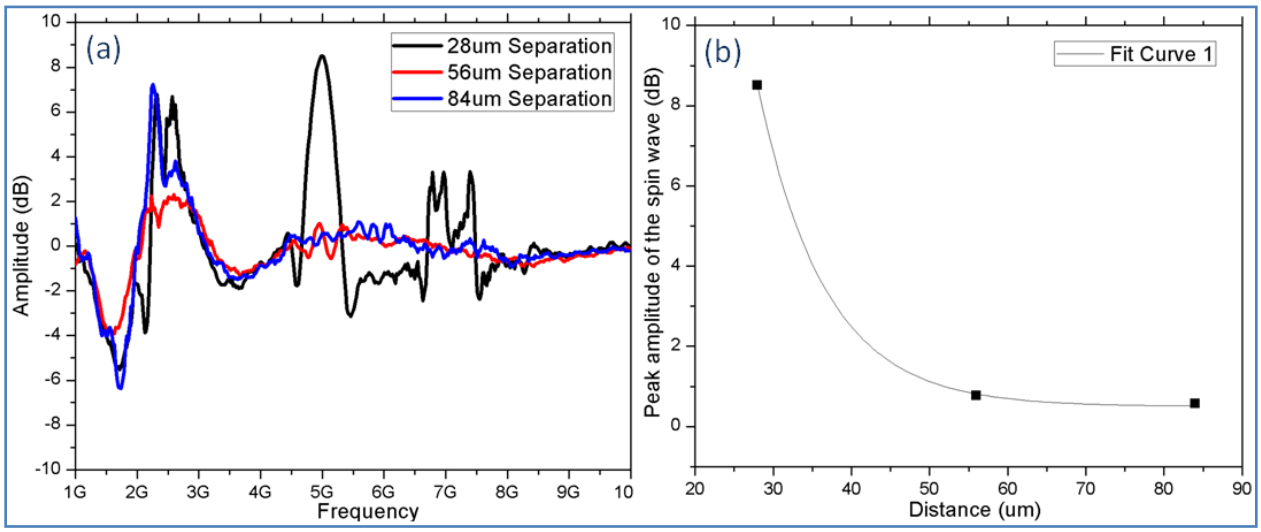

Figure 3.13: (a) Spin wave transmission plots at 400Oe. The colors indicate different antenna separations. (b) Exponential decay of 5GHz waves at 400Oe.

3.5 Energy considerations of spin wave generation techniques

The primary motive for using an ME cell based spin wave generation and detection is to reduce the operating energy requirements of the device. This section deals with a brief overview of the energy requirements of both the antenna and the ME cell based devices. In order to quantify and compare the energy requirements of these two different devices, it is necessary to set down certain test criteria. Let us assume that the device consists of a thin Ni/NiFe bus, as

used in our numerical studies. The internal magnetic field of this ferromagnetic stripe is given by[25] :

$$\boldsymbol{H} = \boldsymbol{H}_e - \overleftrightarrow{N}\boldsymbol{M} \qquad (3.7)$$

where $\boldsymbol{H}$ is the internal magnetic field, $\boldsymbol{H}_e$ is the external magnetic field and $\boldsymbol{M}$ is the magnetization. $\overleftrightarrow{N}$ represents the demagnetization tensor. Assuming a tangentially magnetized infinitely thin plate, $\overleftrightarrow{N}$ is given by:

$$N_x = N_y = 0;\ N_z = 4\pi \qquad (3.8)$$

Assuming the magnetization is saturated along the length of the bus under a zero external magnetic field, the total internal field is given as:

$$H = -4\pi M_s \qquad (3.9)$$

where M_s is the saturation magnetization. Taking the average value of M_s for Ni and NiFe, we get a net internal field of $H = 8377\ Oe$, directed along the length of the bus, as shown in Fig. 3.14.

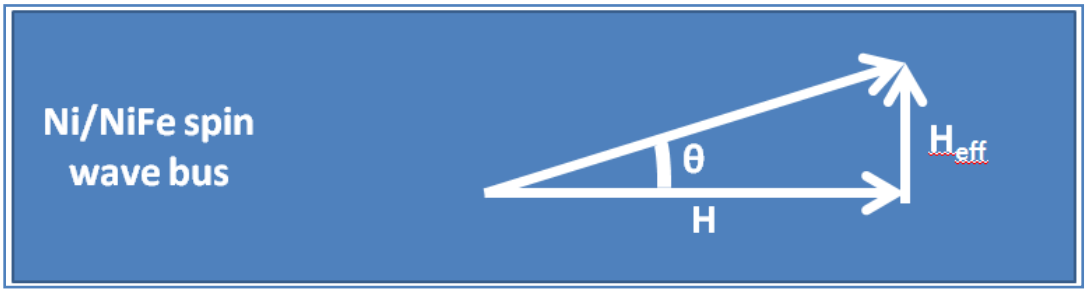

Figure 3.14: Schematic of the spin wave bus indicating the internal and the effective magnetic field. Also shown is the angle of internal magnetic field deflection, θ.

Now, for a spin wave to be generated, the magnetization has to deflect from its relaxed state. To generate a wave which deflects the internal field by a small angle, $\theta = 1^0$, we need to apply an effective field, $\boldsymbol{H}_{eff}$, as shown in Fig. 3.14. This effective field is given by:

$$\tan\theta = \frac{\boldsymbol{H}_{eff}}{\boldsymbol{H}} \qquad (3.10)$$

From the above equation, we can determine the effective field to be 146 Oe. This is the external field that has to be applied to create a spin wave which deflects the magnetization by 1^0. Now let us determine the energy required to generate this field in either case.

In case of an antenna structure, with a cross section shown in Fig. 3.15, the generated field can be determined from the Ampere's circuital law. This field can be approximated as:

$$\boldsymbol{H}_{ant} = \frac{\boldsymbol{I}}{2\pi \boldsymbol{r}} \qquad (3.11)$$

where $\boldsymbol{H}_{ant}$ is the magnetic field generated by the antenna, which should be equal to $\boldsymbol{H}_{eff}$ to generate the required spin wave. $\boldsymbol{I}$ is the current flowing through the antenna and $\boldsymbol{r}$ is the distance between the antenna and the location where the field is measured. $\boldsymbol{r}$ can be approximated to be around 220 nm, assuming an ideal device. Substituting these values into eqn. (3.11), we can compute the current required to generate this field to be 16 mA. Now to determine the resistance of this loop antenna of length 2.4 μm, width 200 nm and thickness 100 nm by using the following formula:

$$R = \frac{\rho . l}{A} \qquad (3.12)$$

to be 2.7Ω, assuming the resistivity of gold at 300^0K to be 2.71×10^{-8}Ω.m. From these resistance and current values, we can determine the total energy required to generate the spin waves to be:

$$E = I^2Rt \qquad (3.13)$$

where t is the time period of the pulse. Assuming the frequency of operation to be around 5GHz, we get t = 200 ps. Substituting these values into eqn. (3.13), we get the net energy required by an antenna to generate a spin wave of 1^0 magnetization deflection to be 141 fJ.

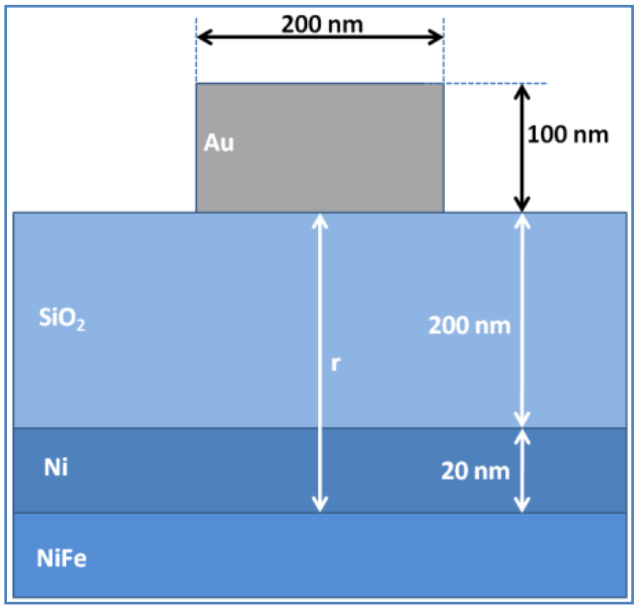

Figure 3.15: Schematic of the cross section of the antenna based spin wave device.

In case of spin wave generation by ME cells, we need to consider the magneto electric coefficient. In our case, this coefficient has been determined to be 10 Oe/kV/cm[52]. Since we need an effective magnetic field of 146 Oe, we can calculate the required electric field to be 14.6 kV/cm. Based on the distance between the inter-digital electrodes of our device, which is 200nm, we can calculate the voltage required to generate this field to be 0.292 V. Also, the capacitance

of the ME cell electrode structure can be approximated as 0.4 fF. From these values, we can determine the energy based on the capacitance model:

$$E = \frac{1}{2}CV^2 \qquad (3.14)$$

This gives a total energy that is required to generate the spin wave using ME cells to be 17 aJ. Hence, comparing the energy requirement of the antenna (141 fJ) with that of the ME cell (17 aJ), it is clearly evident that the ME cell is four orders of magnitude more efficient.

Following a similar approach, we can determine the energy requirement of spin wave generation using micrometer scale ME cells. Considering a distance of 2μm between the IDT electrodes, similar to that of our experimental devices, we can estimate the energy requirement to be 17fJ. Comparing this with the energy requirement of nanoscale ME cells (17aJ), it is evident that scaling down the ME cell structure by a factor 10, leads to three orders of magnitude more energy efficient spin wave generation.

4. Nanoscale Spin Wave Device Design Considerations

The advantages of having a nanoscale device are many. However, we are primarily interested in the ultra low power operation that is achievable through the use of nanoscale ME cell device design. The energy metrics have been discussed previously. In short, in antenna devices, the ohmic losses are high and the power primarily consists of a resistive term. This can lead to energy consumption in the femto joule range. On the other hand, in case of ME cells, the capacitive term is dominant. The capacitance of the ME cell decreases as the size of the device reduces. In turn, the reduction in capacitance further decreases the energy consumption. This is the primary motivation of scaling down the SWD to nanoscale sizes. The energy consumption of the nano-scale devices have been calculated to be in the atto joule range, as presented in the previous chapter. Further, the characteristic frequency of the IDT, given by $f_o=v/d$, has an inverse

relation with the pitch of the device[53], d, with v being the velocity of the SAWs in PMN-PT. In case of our nano devices, with $d=400nm$ and $v=5500m/s$ [54], the characteristic frequency of the IDT is 13.75 GHz. Hence, the frequency of the SAWs can be shifted higher, into the gigahertz regime, by scaling down the device. This leads to more effective coupling with the gigahertz spin waves. In essence, scaling the device leads to better generation and detection of spin waves due to better coupling between SAWs and spin waves. Also, scaling the device to nanoscale length scales leads to the dominance of the short range exchange interactions. This would enable the generation of high frequency, exchange dominated spin waves. With these vast benefits in mind, in order to design our nano SWD, it is imperative to decide upon certain material and device parameters.

4.1 Material considerations in the device design

Material characterizations were performed on devices excited by GSG antennas, shown in Fig. 4.1. We measured the transmission and reflection coefficients on devices with NiFe, NiFe/Ni bi-layer or Ni stripes. Spin waves were excited and detected using GSG antennas. From these characterizations shown in Fig. 4.2, it is evident that the strongest transmission signal is attained in the case of NiFe bus (Fig. 4.2a), since the spin wave damping is the least in NiFe. The Ni/NiFe bi-layer (Fig. 4.2b)

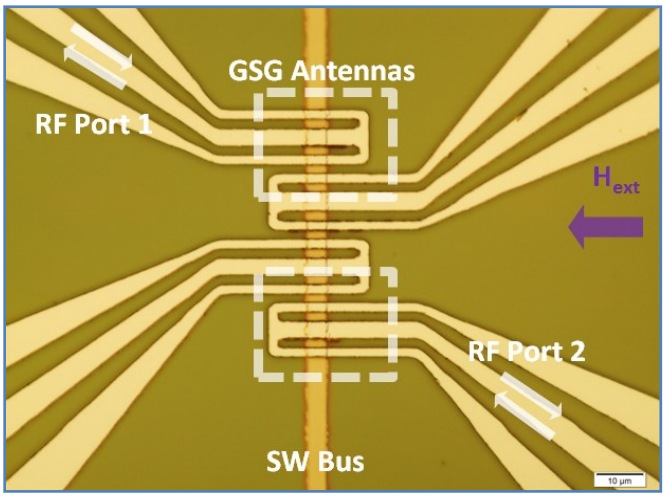

Figure 4.1: Optical micrograph of the device used for material characterizations. The device consists of a stripe of the material to be characterized, patterned on a silicon substrate. The spin waves are generated and detected using aluminum/titanium GSG antennas.

has slightly weaker transmission signal due to the spin waves in the NiFe layer being exchange coupled to the waves in the Ni layer. In case of Ni bus (Fig. 4.2c), we do not see any spin wave signal due to the high damping in Ni. It has to be noted that these characterizations were performed using inductively coupled antennas. In case of devices excited using ME cells, the Ni/NiFe bi-layer is the most suited.

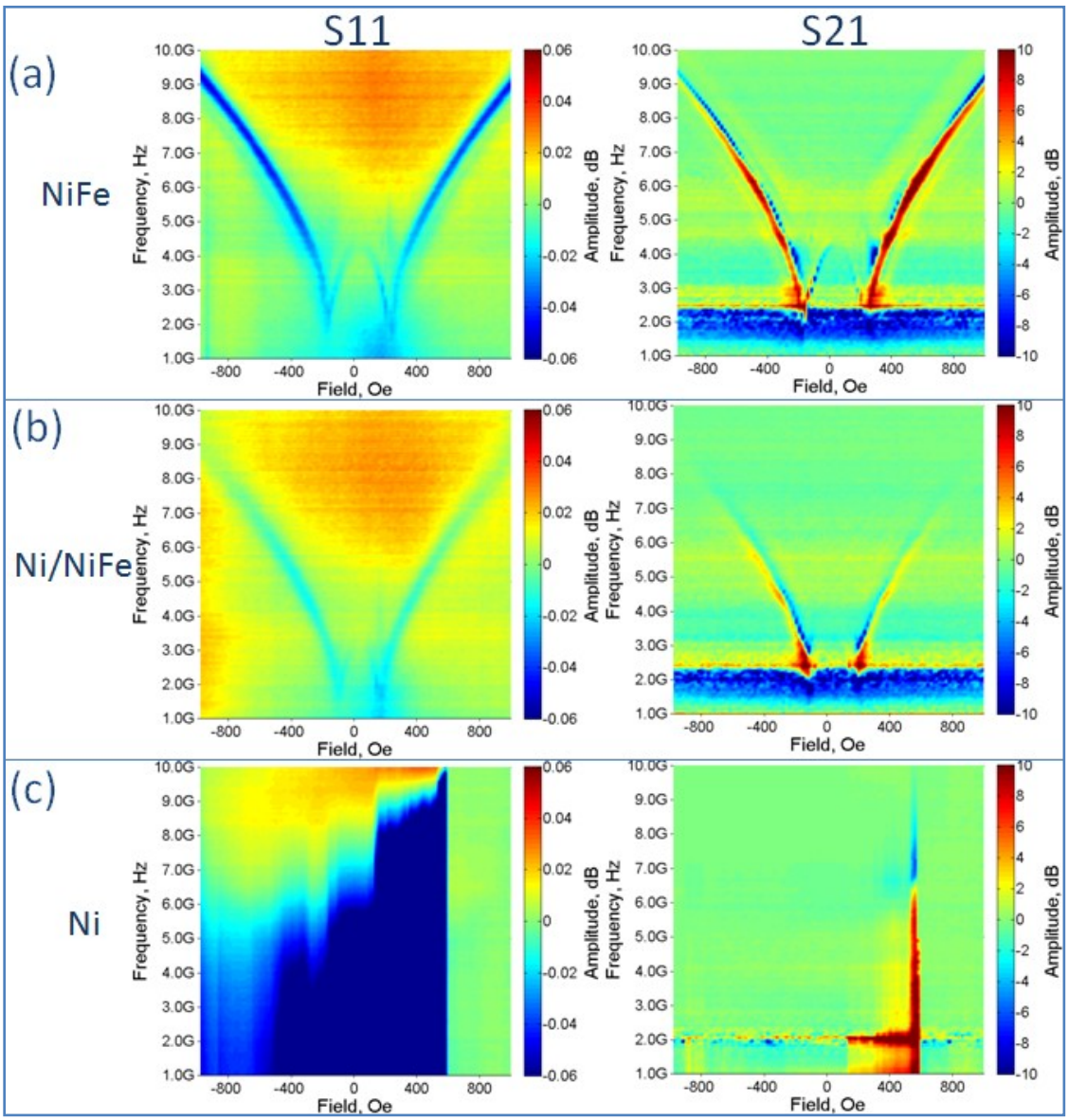

Figure 4.2: S - parameters of devices with (a) NiFe (b) Ni/NiFe (c) Ni stripes. The colors indicate the amplitude of the scattering parameter. It is evident from these plots that the spin wave decay is the least in NiFe.

4.2 Study of the spin wave modes of the device

To understand the spin dynamics in these devices, we need to consider the non uniform solutions of the LLG equation. These non uniform solutions define the spin wave modes in a system. In the general case of bulk material with no confinements, the spectrum of spin waves can be obtained by the simultaneous solution of the equation of motion of the magnetization and the Maxwell's equations[55]. In case of continuous thin films, the confinement along the thickness of the film should be considered while solving the set of equations[56–58]. This confinement leads to discrete branches in the spin wave spectrum[57,58]. It also leads to quantization of the wave vector perpendicular to the film.

In this case of continuous thin films, the spatially uniform solution of the LLG equation, in which all spins precess in phase, is given by the Kittel's equation[59]. These spin waves with zero wave vectors can be easily observed using the ferromagnetic resonance technique. Griffiths was the first to observe the uniform spin precession, using this technique, in 1946[60]. For the spatially non uniform solutions, the type of interaction between the spins determines the characteristics of the spin wave. The 'slow' waves with small phase and group velocities have high wave numbers, enabling us to neglect the dynamic part of the Maxwell's equations[25]. The solutions of the LLG equation based on the magnetostatic dipolar field are called the magnetostatic waves. The dispersion of these waves can be derived from the Walker's equations[61]. Due to the longer wavelength, these waves depend only upon the long range dipolar interaction and are called dipolar or non-exchange magnetostatic waves. The dipolar interactions being anisotropic, these waves have an angular dependence.

Consider an in-plane (tangentially) magnetized continuous film with a magnetostatic potential given by[25]:

$$\psi = (A\cos k_x x + B\sin k_x x)\exp(-ik_y y - ik_z z) \qquad (4.1)$$

Where A and B are constants, k_x, k_y and k_z are the wave vectors along x, y, z directions respectively. Here x is normal to the film and y, z are tangential to the film. y is normal to M_0 and z is along the direction of M_0. When the direction of propagation is along the magnetization (k || $\boldsymbol{M}$), there exists volume waves with a precessional frequency smaller than that of the uniform precession case. The dispersion of such waves are given by[25]:

$$\omega = \gamma\sqrt{H_0\left(H_0 + \frac{4\pi M_0}{1+\frac{k^2d^2}{n^2\pi^2}}\right)} \qquad (4.2)$$

Where ω is the precessional frequency, γ is the gyromagnetic ratio, H_0 is the steady state magnetic field, M_0 is the steady stage magnetization, n is the number of half-waves of ψ in the confined direction, k is the wave vector along M_0 and d is the thickness of the film. This leads to a negative dispersion in which the frequency reduces with increasing wave number and the group velocity is anti-parallel to the wave vector and the phase velocity. Hence, these waves are called backward volume magnetostatic waves[25]. A similar scenario, though for a laterally confined medium in the form of a strip, is shown in Fig. 4.3a. It shows a NiFe strip magnetized along its length by applying an external magnetic field in the same direction. When a spin wave is generated using GSG antenna, it propagates along the length of the strip, i.e. k || $\boldsymbol{M}$. The figure also contains the S – parameters.

In the case of ($k \perp \boldsymbol{M}$), when the direction of propagation is perpendicular to the magnetization, the waves are localized on the surface of the film and have a positive dispersion relation given by[25]:

$$\omega = \gamma\sqrt{\left(H_0 + \frac{4\pi M_0}{2}\right)^2 - \left(\frac{4\pi M_0}{2}\right)^2 \exp(-2kd)} \qquad (4.2)$$

These waves are known as Damon-Eshbach magnetostatic waves[62]. This scenario is similar to the one shown in Fig. 4.3b, where a bias field is applied along the width of the bus. When spin waves are generated using GSG antennas, they propagate along the length of the bus, i.e. $k \perp \boldsymbol{M}$. The figure also shows the S - parameters.

Since the antennas are aligned in the same direction in both cases, a fair comparison cannot be made regarding the amplitude of these waves. This is evident in the comparison of S11 plots, which indicate that the ferromagnetic resonance is weaker in the former. However, the magnetic field dependent resonance frequencies can be compared. It is seen that the resonance frequency is higher when the magnetic field is applied along the length of the bus. This can be explained based on the fact that the effective magnetic field is the vectorial sum of the external magnetic field and the anisotropy field. Hence when they are aligned, as in the former, the net magnetic field is larger, leading to higher resonance frequency.

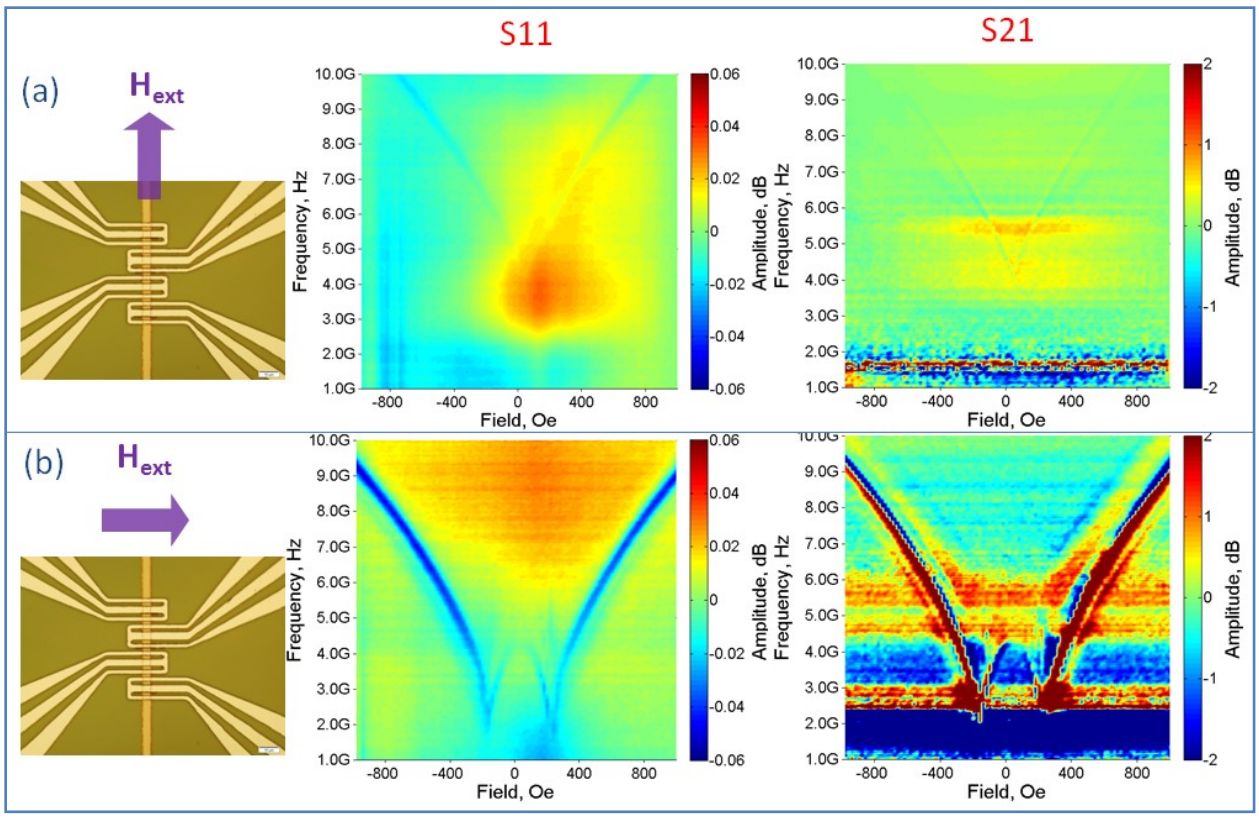

Figure 4.3: Experimental study on spin wave modes. The device geometry and the S - parameters are shown in this figure. By applying the external magnetic field in different direction, we can excite different modes. (a) Field applied along the bus, exciting backward volume waves primarily. (b) Field applied perpendicular to the bus, mainly exciting Damon-Eshbach modes.

For all intermediate angles between the wave vector and the magnetization, the dispersion is negative. The schematic dispersion curves are shown in Fig. 4.4[11]. For spin waves with lower wavelengths, the exchange interaction can no longer be ignored and we get dipole-exchange spin waves, in which both the long range dipolar interaction and the short range exchange interaction has to be considered[58].

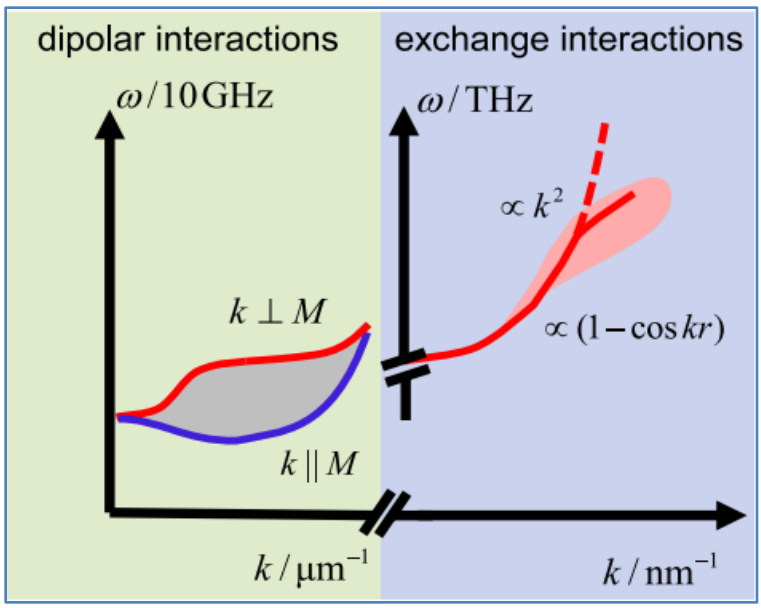

Figure 4.4: Schematic spin wave dispersion curves. At longer wavelengths, dipolar interactions are dominant and the waves are of lower frequency. As the wavelength decreases, the short range exchange interactions become more dominant, leading to terahertz spin waves. Illustration obtained from ref. 11.

At much lower wavelengths, the long range magnetostatic dipolar field can be ignored and the wave dispersion depends primarily on the short range exchange interaction. These waves are called exchange spin waves. The dependence on exchange interaction leads to an increase in the frequencies of these waves with growing wave number. These high energy spin waves are heavily damped with short life times. Further, since the exchange interaction is isotropic, the angular dependence of dispersion is not seen in this case, unlike magnetostatic waves. The generalized dispersion relation of spin waves was given by Holstein and Primakoff[31].

4.3 Studies on the nano-scale device parameters

Based on the experimental results of the previous sections, we conducted numerical studies on different device structures. It can be seen that in case of Ni stripe (Fig. 4.5a), the generated spin waves are highly damped and are not detected at the output.

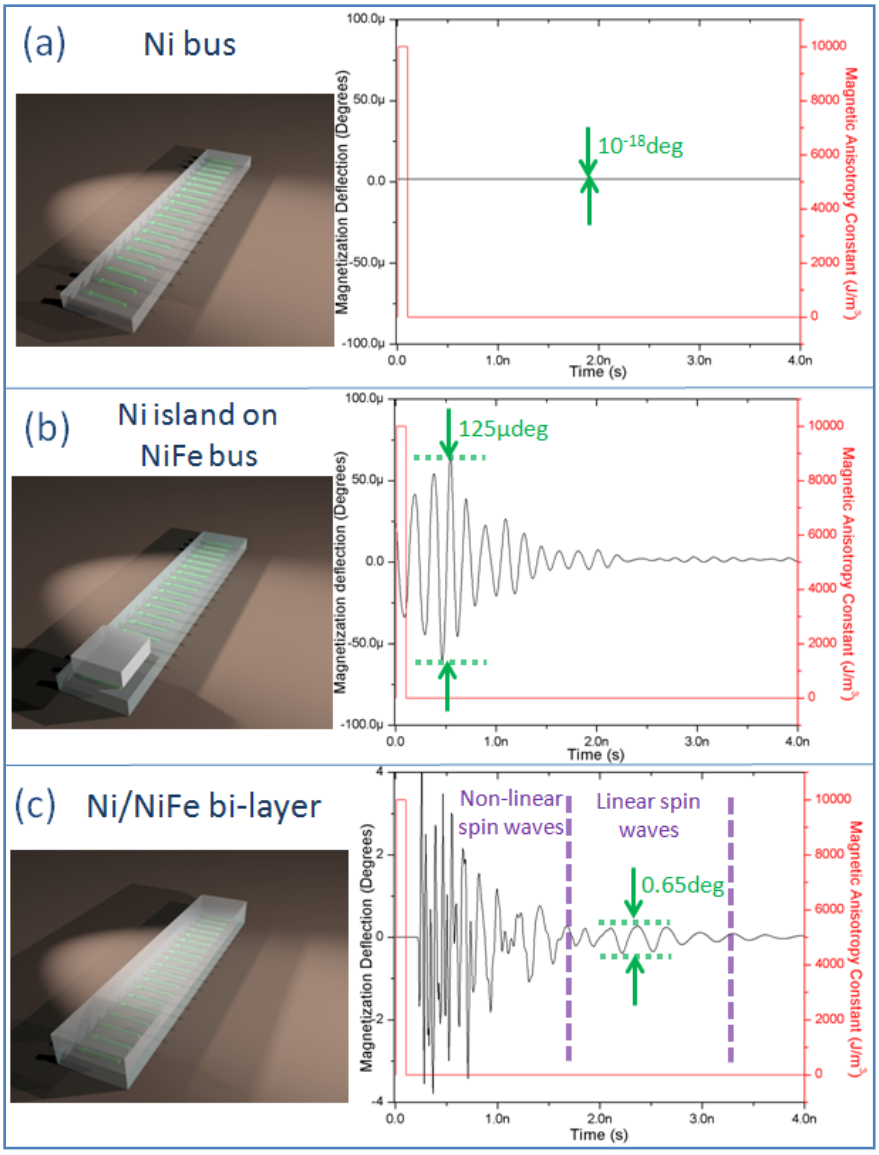

Figure 4.5: Numerical studies on different device structures. The device schematics and the results are shown for (a) Ni Bus (b) Ni island on NiFe bus (c) Ni/NiFe bi-layer. In the plots, the black lines indicate the rotation of the magnetization vector in degrees while the red line indicates the input square pulse. It is evident that the bi-layer is most suited for efficient spin wave generation using magneto electric effect.

In case of Ni/NiFe bi-layer (Fig. 4.5c), exchange coupled spin waves propagate in the bi-layer structure and are detected at the output. This structure provides a greater magnetization deflection at the output, than the structure, shown in Fig. 4.5b, consisting of a Ni island exchange coupled to a NiFe bus. This is most likely due to the effects of surface anisotropy and the magnetization configuration on the spin wave generation and propagation.

We also performed numerical studies to determine the device geometry. Figure 4.6 shows the FFT magnitude of the generated spin waves at the output. It can be easily discerned that the FFT magnitude, at resonance frequency, is maximum in smaller bus widths.

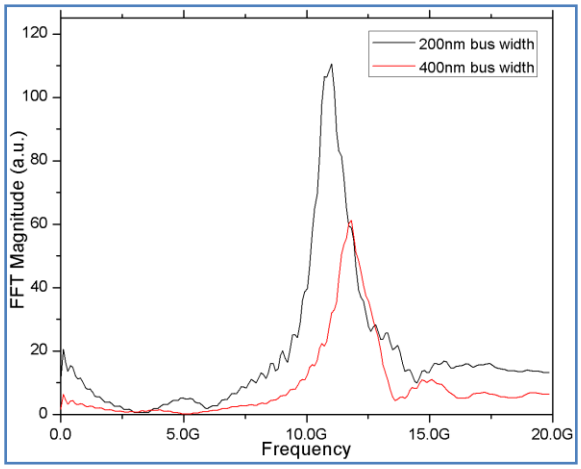

Figure 4.6: FFT magnitude of spin waves in numerical models with different bus widths. The black line corresponds to 200nm bus width and the red line corresponds to 400nm bus width. Stronger spin wave is generated as the width of the bus is decreased.

For non-ellipsoidal shapes, the lateral confinement leads to the modification of the internal fields, due to demagnetization effects[63,64]. It was determined that the demagnetizing field causes the magnetization to become less saturated at the edges, as the bus width decreases. The magnetization configuration of this device is shown in Fig. 4.7a. The arrows indicate the magnetization and the colors indicate the out of plane component of the magnetization. The high

inhomogeneity of the internal field at the edges of the stripe creates a potential barrier along the length of the strip. This leads to multiple wave modes along the longitudinal edge of the stripe. These exchange dominated, spatially localized edge modes are called spin wave wells[65–67].

The edge modes are further illustrated in Fig. 4.7b, which shows the spatial profile of the amplitude of the resonance mode. These spin wave wells provide a medium for the localized, exchange dominated spin wave propagation. To obtain this plot, spectral analysis was performed on the data from every individual micromagnetic cell. This spectral data were then used to plot the waves at the characteristic frequency of the device. All these post processing on the numerical data were performed using Semargl[68].

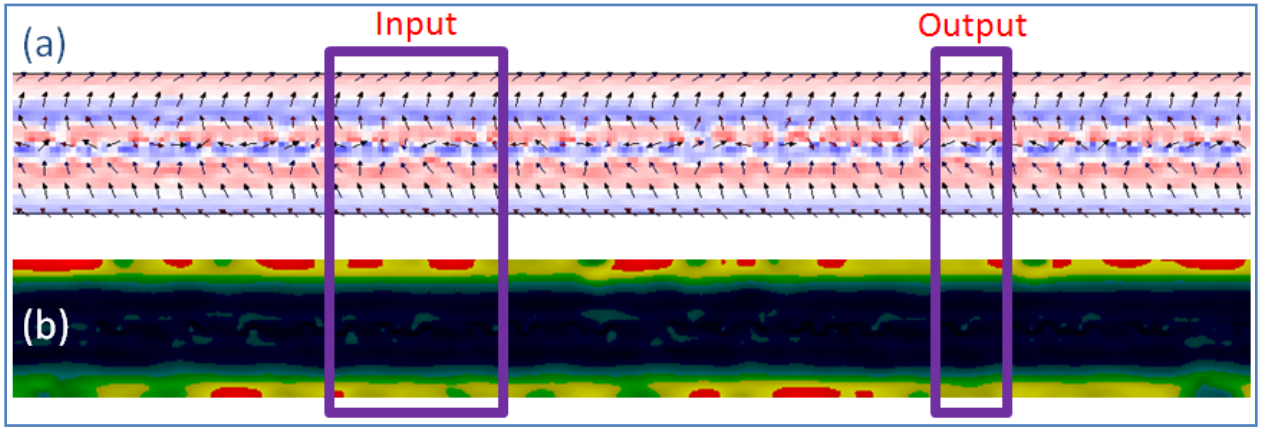

Figure 4.7: (a) The magnetization configuration of the device. The arrows indicate the direction of magnetization and the red and blue colors indicate the out of plane component of magnetization. The horizontal spin wave wells are clearly visible. (b) Spatial profile of the amplitude of the resonance mode, indicating the presence of edge modes. The spatial distribution was determined using the post processing tool Semargl (ref. 68).

5. Design Summary of the Nanoscale Spin Wave Devices

Our proposed device design, as shown in Fig. 5.1, consists of a ferromagnetic double-layer Ni/NiFe strip patterned on a piezoelectric PMN-PT substrate. We use inter-digital transducer (IDT) electrodes to locally excite surface acoustic waves (SAW). These acoustic waves can in turn generate spin waves due to the magnetostrictive property of Ni. The periodicity of the IDT fingers determine the frequency of operation of the SAW generator[44,45,69]. Other considerations such as the required aperture and the number of IDT fingers to maximize coupling to the substrate; spacing between IDTs to minimize electromagnetic coupling etc[69] were taken into account while designing the IDT. The IDT used in our nanoscale design were of 3 electrodes, with a width of 200nm and a pitch of 400nm. In order to localize the effect of the IDT, it was placed at a distance of 100nm from the spin wave bus. The short distance also

ensured that the SAWs do not attenuate before reaching the bus. The IDT electrodes along with the local spin wave bus constitutes the ME cell.

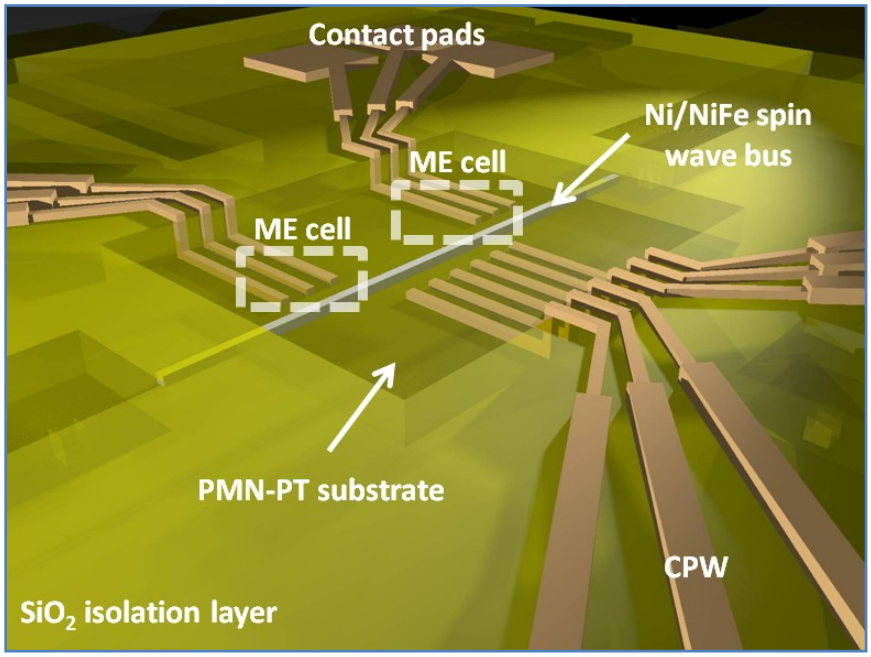

Figure 5.1: Proposed design of the nanoscale Spin Wave Device. The device consists of a patterned Ni/NiFe strip on a PMN-PT substrate. The spin waves are generated and detected using CPWs terminated in IDTs. The CPWs are isolated from the PMN-PT substrate using a thick SiO_2 layer.

The SWD can be connected to an RF signal source, in our case a Hewlett Packard 8722ES Vector Network Analyzer (VNA), using high bandwidth surface probes connected to the contact pads. The contact pads are connected to the IDTs via coplanar waveguides (CPW). A CPW is fabricated on a dielectric substrate with a center signal stripe with wide ground planes on either sides. It has several advantages over other types of waveguides[70]. Our CPW design was optimized to reduce noise in the measurements, from signal reflections, interference between different CPWs etc. The widths of the stripes were increased in order to reduce the resistance of the CPW. The increased width of the ground strip also ensured that the crosstalk between different CPWs was minimized. Further, the distance between the signal and ground lines was

minimized to optimize the CPW performance, since the characteristic impedance of a CPW depends on the ratio of half-width of the signal line to the distance between the ground lines. Another design criterion to be addressed was the case of CPW bends. Two options considered by us were mitered bends and meandered bends[70,71]. We opted to use sub-micrometer-sized meandered bends, in order to minimize signal reflections[72]. All the design parameters for the CPWs were based on rough calculations[70]. Thus, the input and output channels in our design consist of open circuit CPWs terminated in IDTs.

Material properties play an important role in the effective generation of spin waves using SAWs via the magneto electric effect. For high ME coupling, the spin wave bus should have a large magnetostriction coefficient λ_S. At the same time, it should have a low damping coefficient α and a small coercive field H_c to aid in spin wave propagation. The saturation magnetization M_s has to be optimized too, since a lower M_s leads to a higher ME coupling, while a larger M_s increases the bandwidth of the SWD[73]. The soft, low loss, high M_s NiFe is an ideal candidate for spin wave propagation; while the high magnetostriction, low M_s Ni is a good ME material. Hence, the spin wave bus is designed as a bi-layer of exchange coupled Ni and NiFe. The bus has a width of 200nm and each layer is 20nm thick. Such bi-layer systems have been studied previously[47,74]. The interlayer exchange coefficient and the film thickness play a huge role in the magnon dispersion curves of such systems. The spin wave frequency, in general, increases with decreasing thickness of the film. Further, with increasing interlayer exchange, each exchange mode splits into symmetric and asymmetric modes[74]. This is analogous to the case of diatomic lattice phonons. The frequency of such modes is also shifted higher. Another point to be noted here is that, even though the ME cell is designed to excite spin waves, if the

spin waves and the acoustic waves of same wave number have comparable frequencies, magnon-phonon coupling can occur. This can lead to coupled magneto-elastic waves[75–78]. Hence, the energy efficiency of the system depends on the SAW-spin wave coupling in such cases. By scaling down to nanometer length scales, the frequency of SAW can be increased to gigahertz range, increasing this SAW-spin wave coupling.

Once the spin waves are generated in the bi-layer due to the stress induced anisotropy rotation, it propagates in the spin wave bus and is picked up by a symmetric ME cell. Using ME cells with similar structure ensures that they are tuned to the same bandwidth. This in-turn leads to high frequency selectivity. This way, the propagating spin wave spectroscopy (PSWS) technique can be applied to the SWDs.

We have fabricated nanoscale devices with IDTs as well as loop antennas which are inductively coupled to the magnetic stripe, to characterize the structures using the PSWS technique[16]. One criterion which we had to address before the fabrication was the electric polling induced anisotropy rotation[79]. This rotation can result from the deliberate polling of the substrate or the polling occurring during the fabrication processes. The nanofabrication process flow is detailed in the next chapter.

6. Nanofabrication of Spin Wave Devices

From our numerical and experimental studies, we determined a 200nm wide, 20nm thick stripes of Ni and NiFe in a bi-layer structure, to be the most ideal for our primary goal of energy efficient generation of spin waves. We started with a substrate of polycrystalline PMN-PT, as shown in Fig. 6.1. The substrate was polished using Chemical-Mechanical Planarization (CMP) technique. Since we start with a polycrystalline substrate, it is necessary to pre-electric poll the substrate as well. It is then necessary to create markers on the substrate, in order to

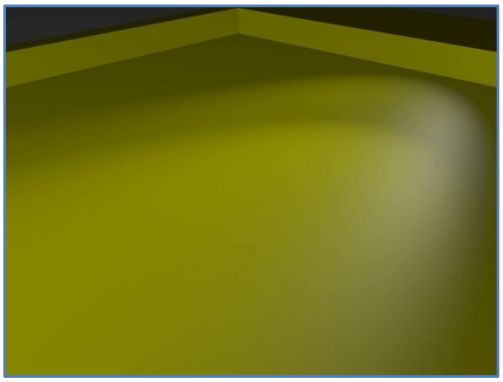

Figure 6.1: Schematic of the PMN-PT substrate.

perform the subsequent e-beam steps. But since the substrate that we used consisted of elements from across the periodic table, we could not use the standard gold or aluminum markers. This is because the atomic weights of these elements would be comparable to those of the constituent elements of our substrate. Hence, these would not show the required contrast in the back-scattering electron detector of our e-beam lithography system Therefore we resorted to using etched markers on the substrate, as shown in Fig. 6.2. This had the unintended consequence of having markers with a wide, irregular side wall. The markers were defined using photolithography, using the equipment shown in Fig. 6.9a. We used a thick photo resist which was prepared by spin coating AZ 4620 at 7000rpm for 30 seconds and then baking it at 100^0C for 1 minute. The sample was then etched in a chlorine etch system. Care has to be taken not to over-etch, in order to prevent the resist from burning.

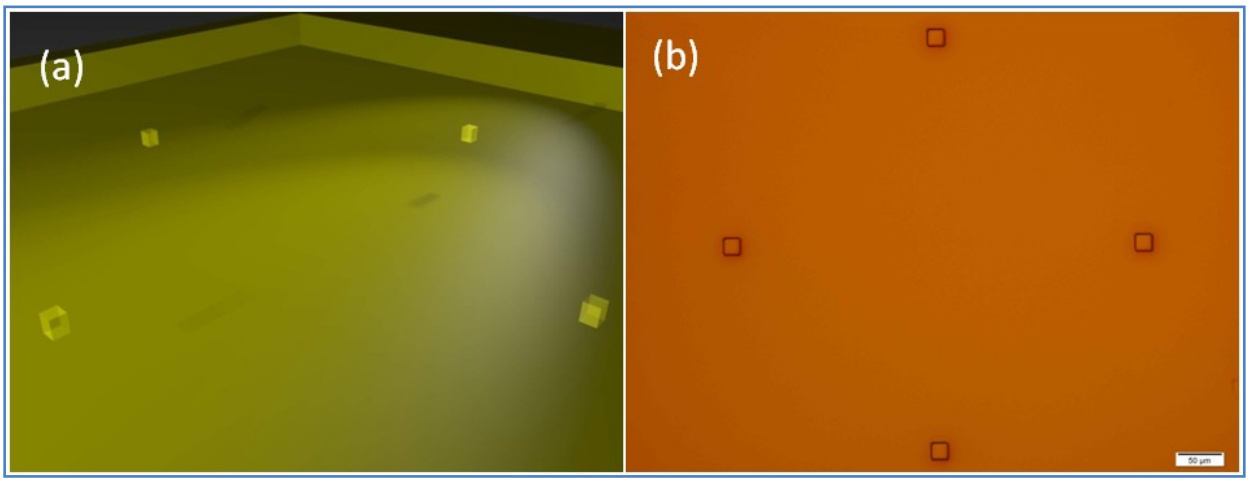

Figure 6.2: (a) Schematic and (b) optical micrograph of the etched markers on the PMN-PT substrate.

Once the markers were etched, the e-beam lithography of the 200nm wide Ni/NiFe bus was performed, as shown in Fig. 6.3a. A standard double layer e-beam lithography recipe was used for the resist, which consisted of spinning on Poly (methyl methacrylate) - PMMA – 495A4

at 2000rpm and then soft baking it at 180^0C for 2 minutes; then spinning on PMMA – AZ950 at 2000rpm and then soft baking it at 180^0C for 2 minutes. A thin 20nm layer of gold was also sputtered on, to make the surface conductive. The resist was then exposed using the e-beam with a dosage of 850 $\mu C/cm^2$ and a beam current of 5nA. The image of the Vistec e-beam writer is shown in Fig. 6.9b. Performing the e-beam alignment was tricky since the substrate would charge up and markers were not usable continuously for a long time. The uneven profile of the marker also caused difficulty in alignment. After exposure, the resist was developed and a 20nm thick NiFe layer was sputtered on, using the sputter shown in Fig. 6.9c. A 20 nm layer of Ni was then deposited on top using e-beam evaporation technique. The Ni e-beam evaporator is shown in Fig. 6.9d. Figure 6.3b shows the image of the spin wave bus under a scanning electron microscope (SEM). Since the substrate is insulating, the image is not very clear. The image of the SEM is shown in Fig. 6.7e.

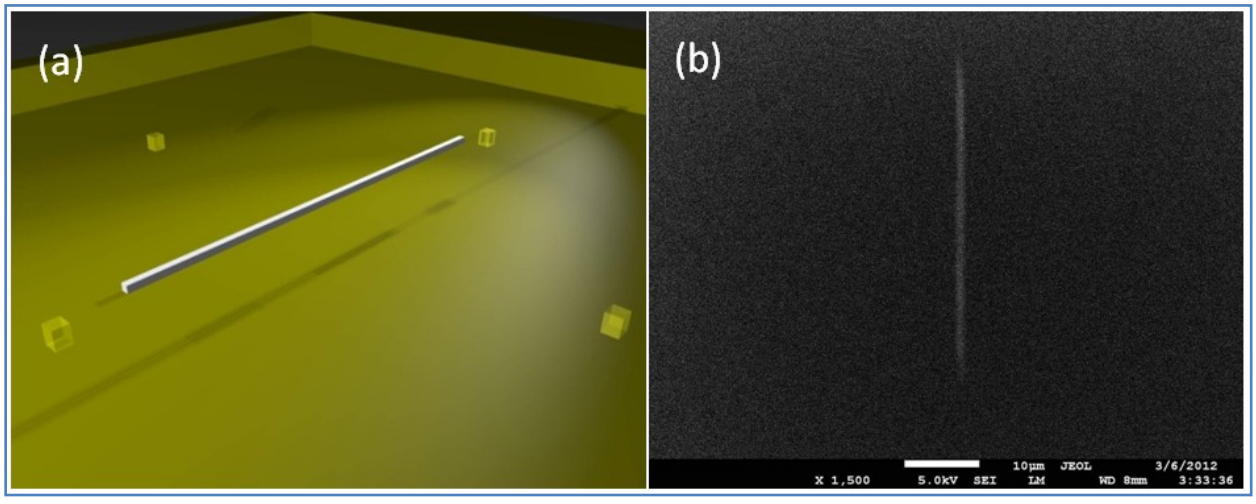

Figure 6.3: (a) Schematic and (b) Scanning electron micrograph of the patterned Ni/NiFe stripe.

Once the spin wave bus was fabricated, a 200nm thick layer of SiO_2 was deposited using Plasma Enhanced Chemical Vapor Deposition (PECVD) and the etched down using an SiO_2

asher, as shown in Fig. 6.4. The SiO_2 acts as an isolation layer for the antennas, CPWs and the contact pads.

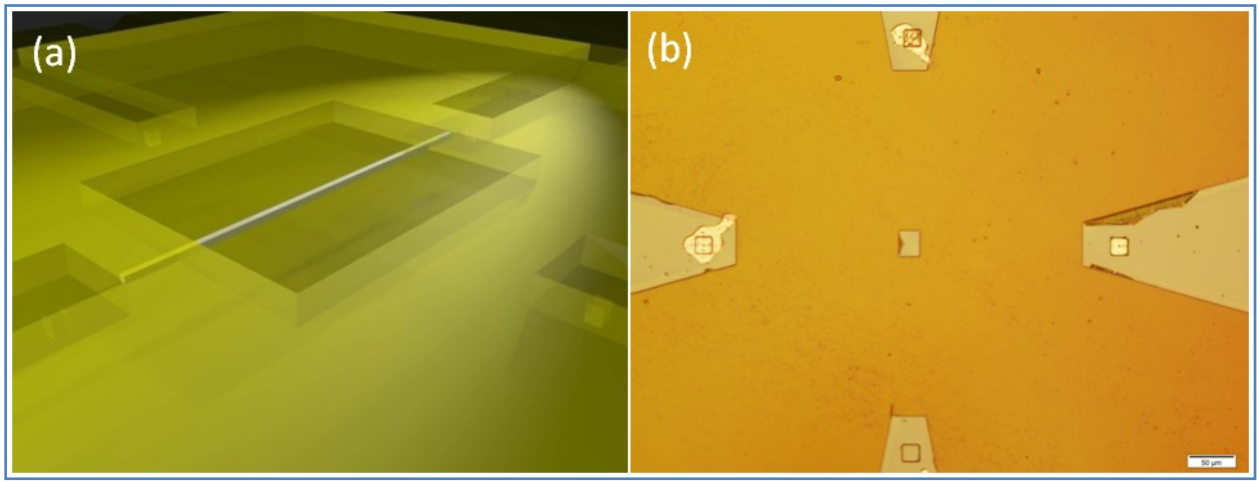

Figure 6.4: (a) Schematic and (b) optical micrograph of the device after SiO_2 isolation layer deposition.

The IDT electrodes were fabricated using e-beam lithography, as shown in Fig. 6.5a. But due to our intricate design, we had to contend with exposure problems. This implied that we had to re-design some of the elements of our IDT electrodes and the connectors to the CPW. We also had to resort to using two different e-beam steps due to the presence of both large and fine features in our design. This led to an alignment issue in the consecutive e-beam steps. This was caused due to software limitations as well as the unpredictability of our alignment markers due to charging. We had to improvise in our use of alignment markers to overcome this problem.

The e-beam was performed using a standard resist and with a dosage of 600 $\mu C/cm^2$ for the larger features and 650 $\mu C/cm^2$ for the finer features. Figure 6.5b, c shows the Critical Dimension – Scanning Electron Microscopy (CD-SEM) images after the development of resist, for both IDT electrodes and antenna structures. These images indicate that the sample was exposed properly.

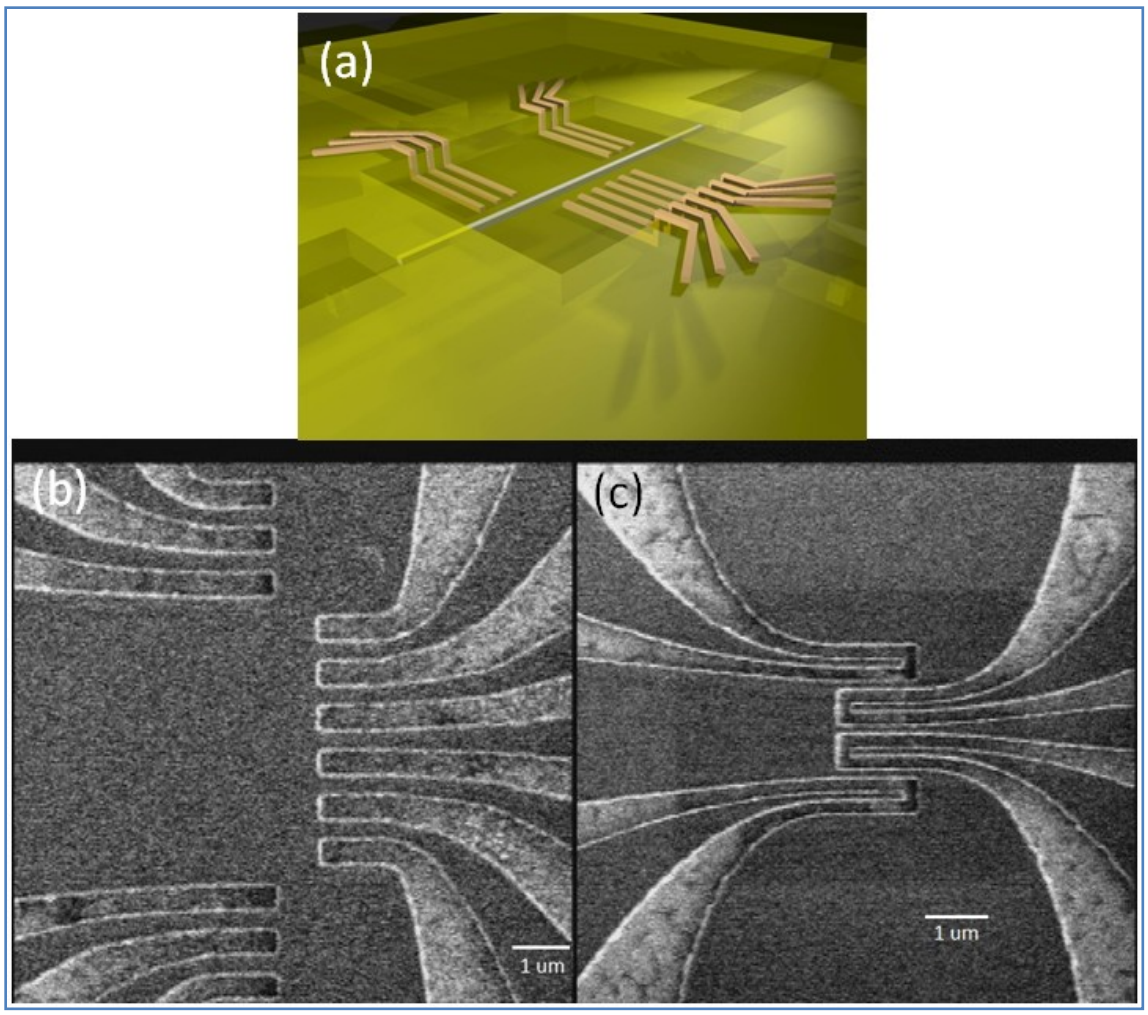

Figure 6.5: (a) Schematic of the IDT electrodes. The CD-SEM micrograph of (b) the IDT electrode structures and (c) the antenna structures, after development of the resist.

After the resist development, approximately 100nm layer of gold was sputtered on. Unfortunately, the metal lift off was not perfect, as seen in the optical micrograph shown in Fig. 6.6a. The CD-SEM images of IDT electrode and antenna structures are shown in Fig. 6.6b, c respectively.

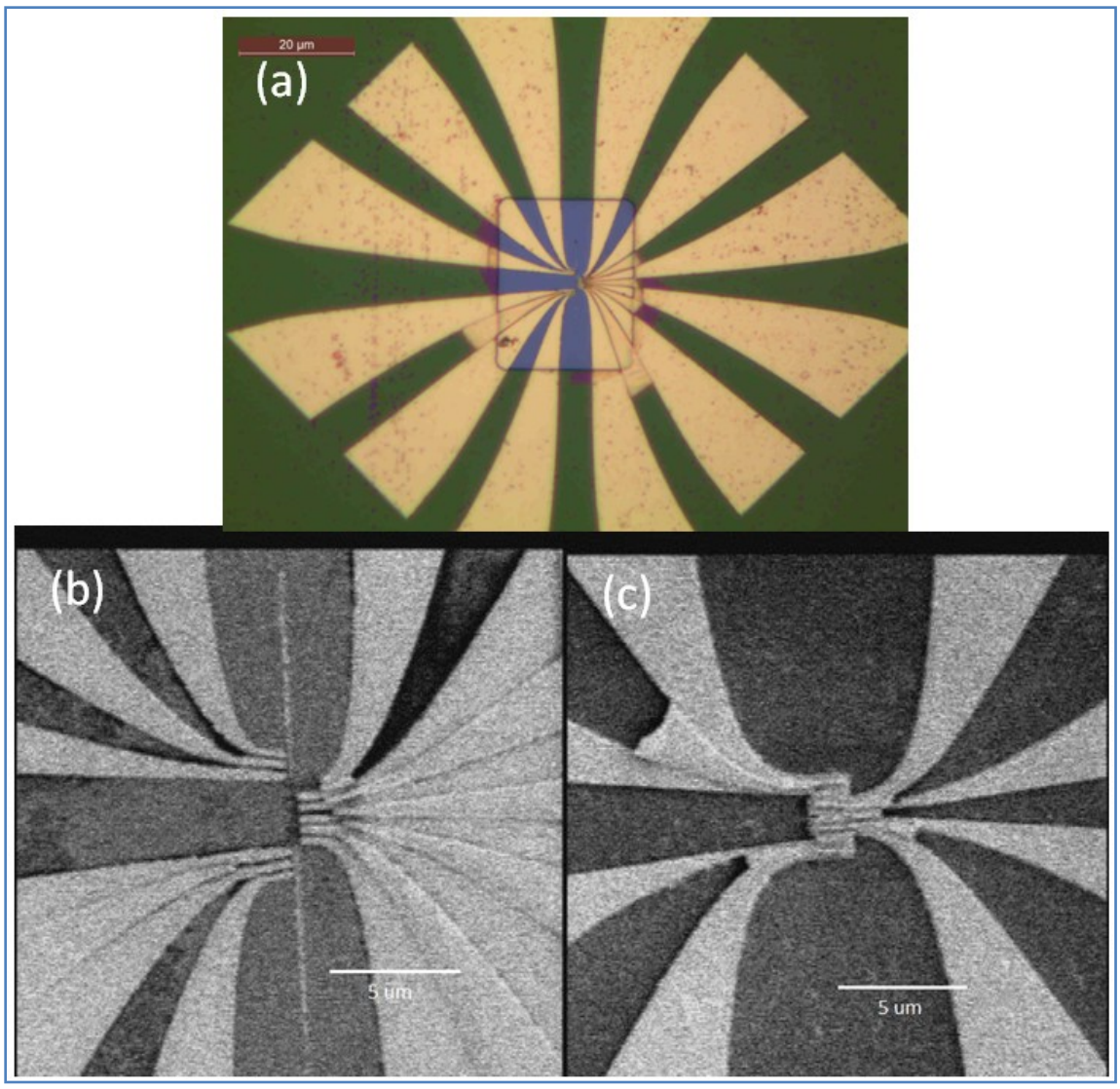

Figure 6.6: (a) Optical micrograph and (b) CD-SEM micrograph of the spin wave device with ME cells. (c) CD-SEM micrograph of the spin wave device with antennas. The gold lift off was not perfect as seen in the images.

Proceeding further, there were two options. One was to use Focused Ion Beam (FIB) to etch the electrodes. The other was to perform another round of gold deposition and lift off. In order to perform FIB, we deposited 100nm of SiO_2 and 100nm of aluminum to make the surface conductive. The SEM image of the ME cell based SWD, after the deposition is shown in Fig. 6.7a. The IDT electrodes were then milled using FIB, as shown in the SEM micrograph of Fig. 6.7b. Figures 6.7c and d shows the SEM micrographs of the antenna based devices, before and

after FIB milling respectively. After the milling, the top layers of aluminum and SiO_2 are etched down and the final step was to deposit a 200nm thick gold layer, for the contact pads, using photolithography.

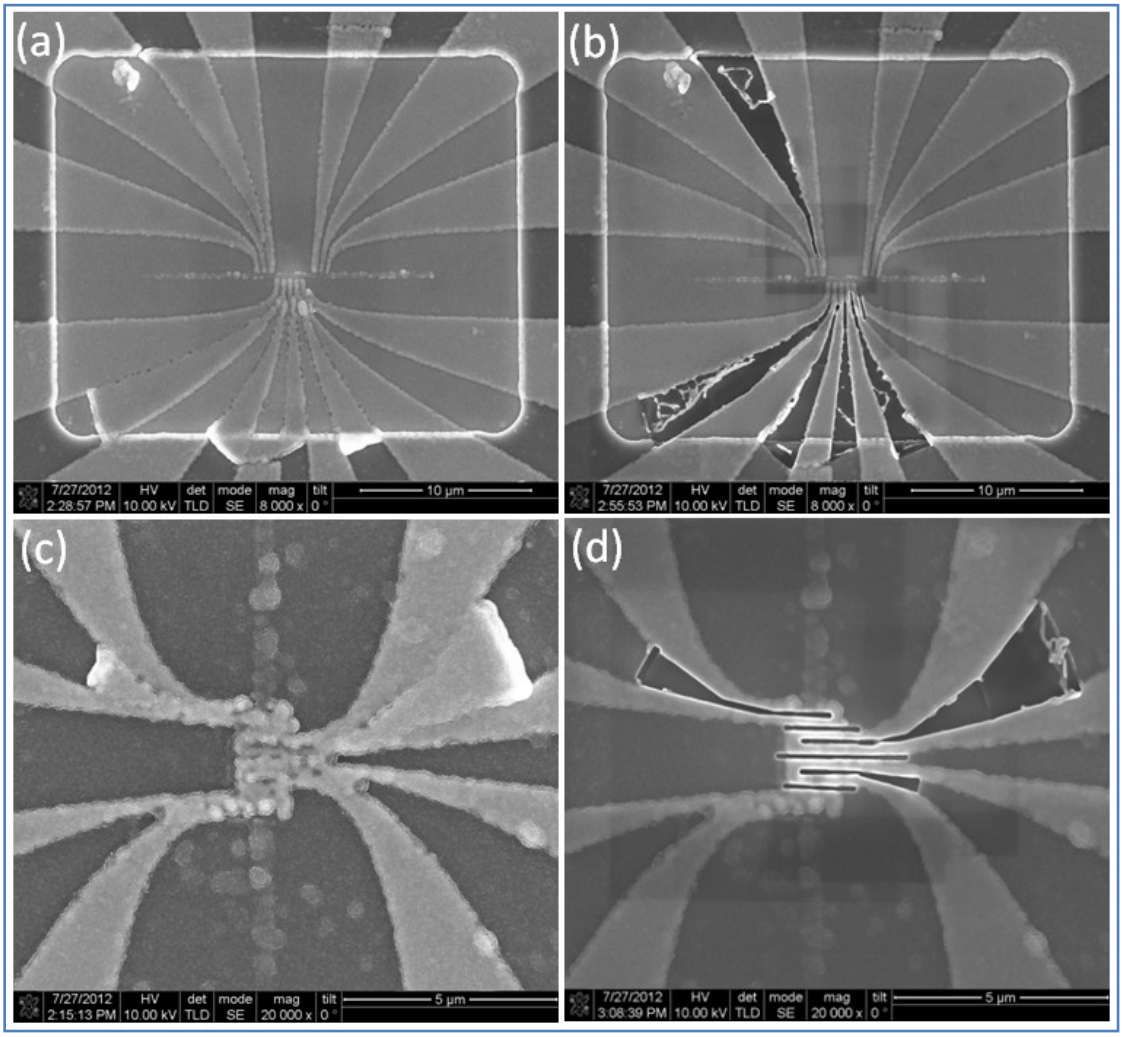

Figure 6.7: SEM micrographs of the ME cell based SWD (a) before and (b) after FIB milling. The SEM micrographs of the antenna based SWD before and after the FIB milling are shown in (c) and (d) respectively.

Schematics of the final devices are shown in Fig. 6.8. The top figure shows a device with ME cells for spin wave generation and detection. The bottom figure shows a device with antennas. These devices are capable of performing majority logic operations.

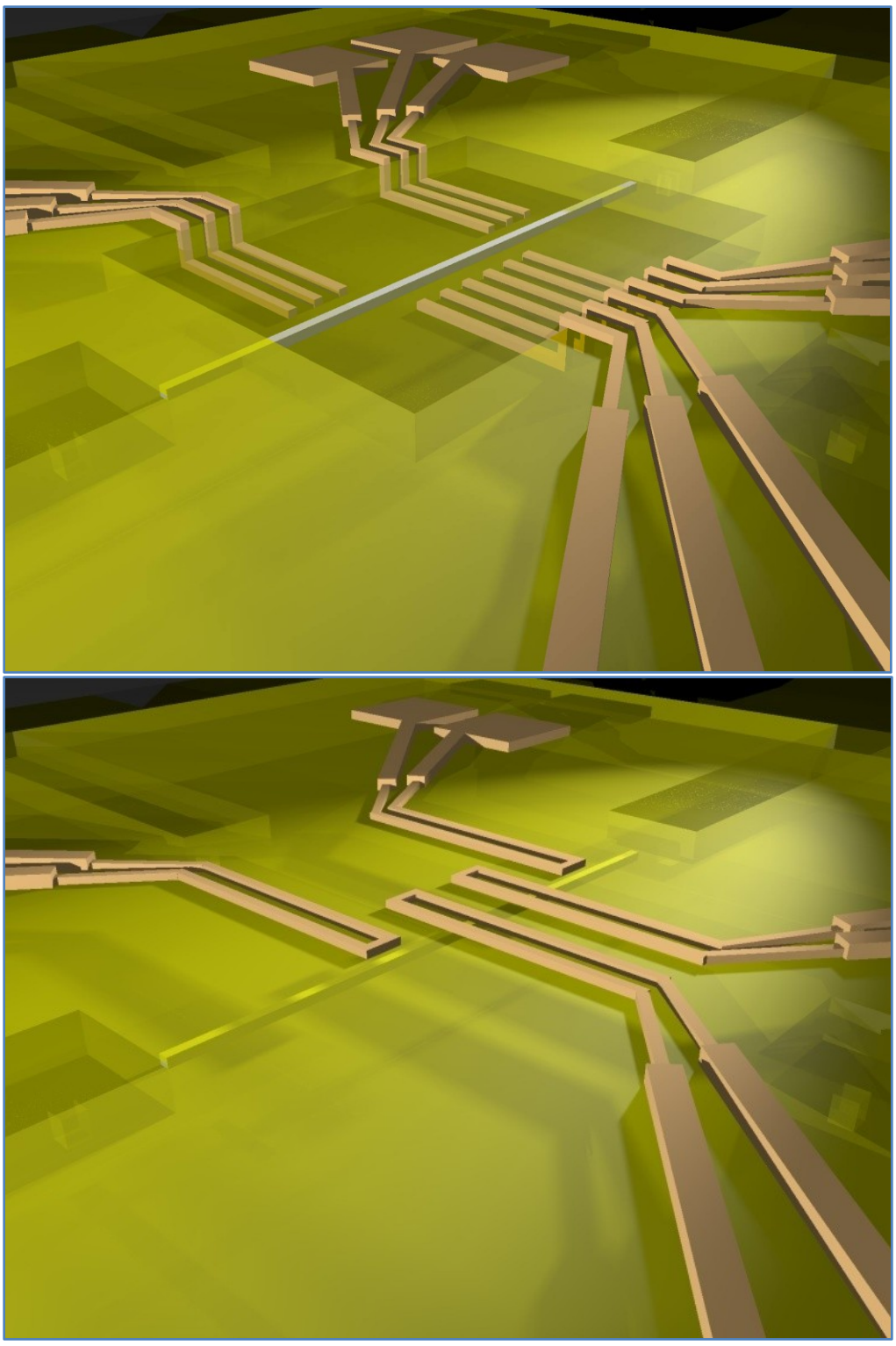

Figure 6.8: Schematic of the nanoscale spin wave device with ME cells (top) antennas (bottom) for spin wave generation and detection.

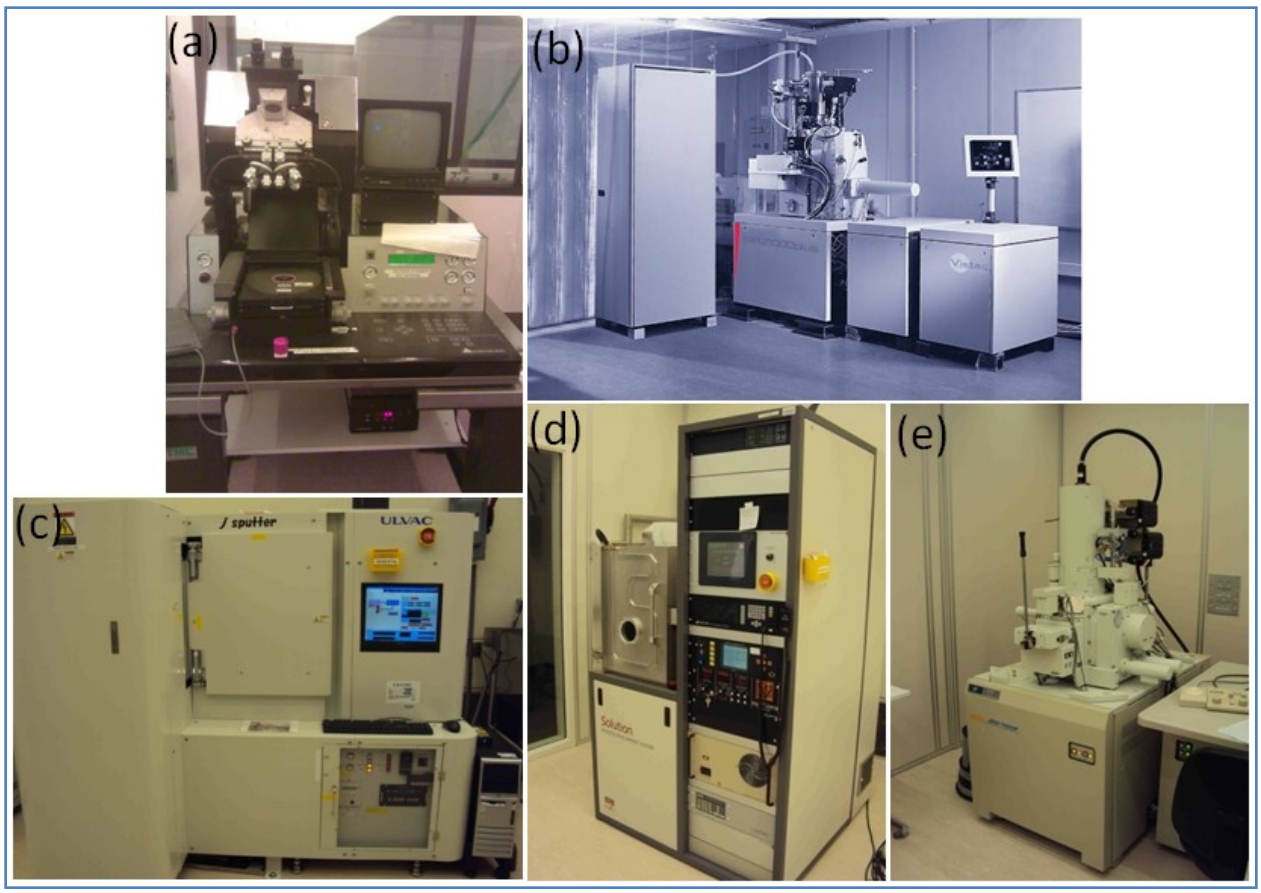

Figure 6.9: Images of nanofabrication equipments used for (a) photolithography (b) e-beam lithography, image obtained from http://www.vistec-semi.com (c) NiFe sputter deposition (d) Ni e-beam evaporation (e) scanning electron microscopy

The fabrication process flow mentioned here is complex. The major challenge that we faced was the alignment of the three different e-beam layers. This problem was exacerbated due to the charging of our substrate under the e-beam. We also faced challenges in proper metal lift off, due to which we had to use FIB milling. To circumvent these problems, we are also pursuing nanofabrication at the 400nm node using stepper, in parallel with this effort.

7. Conclusion

Recently, there has been a lot of interest in magnonic logic as a successor to the current generation CMOS logic. A key aspect in the implementation of the magnonic logic is the generation of spin waves. This study expands on the existing works on the electric field induced manipulation of magnetization and on the magneto-electric tuning of spin waves, to demonstrate the electric field induced spin wave generation using the magneto-electric effect. It is shown that by applying a voltage, the magnetization in a magneto-electric material can be rotated via the strain coupling of the ferromagnetic and the ferroelectric phases. This magnetization rotation leads to the generation of spin waves in the ferromagnetic material. In this work, we presented the design, the numerical studies, the fabrication process flow and the RF characterization results of this energy efficient technique for spin wave generation in magnonic logic devices. We

estimate the energy requirements of these devices to be in the atto-joule range, which is substantially lower than that of the current generation of CMOS devices. Being an exploratory research, there are many aspects of this work which warrants further study.

One of the key works should be on integrating this technology with the current CMOS technologies. This would ensure a faster progression to these exotic devices. Apart from this, the device can be scaled further down from the current 200nm node. This would decrease the power consumption, while pushing the device further into the high frequency regime. We were primarily limited by the fabrication and measurement techniques in this regard. From a circuit level, we need better correlation between the phase of the spin wave and the clocking signals, in order to demonstrate more complex logic devices based on this technology. More work is also required in the field of employing magnetic memory devices along with this logic device, in effect making it non volatile.

We have to conduct further studies to enhance our basic understanding of spin waves. We need to understand in more detail, the effects of surface anisotropy and magnetic super-lattice structures on the surface spin wave modes. We also need to determine ways reduce losses due to eddy currents etc. Further studies of magnon-magnon, magnon-phonon and magnon-photon interactions are also required. The study of magnon-photon interactions are especially interesting, since this could one day perhaps lead to high performance magneto-photonic non volatile logic devices.

Bibliography

1. *ITRS 2011 Edition: Emerging Research Devices*. (2011). Available at : <http://www.itrs.net/Links/2011ITRS/Home2011.htm>
2. Khitun, A., Bao, M. & Wang, K. L. *Journal of Physics D: Applied Physics* **43**, 264005 (2010).
3. Vogt, K. *et al. Applied Physics Letters* **95**, 182508 (2009).
4. Melnikov, A. *et al. Physical Review Letters* **91**, 227403 (2003).
5. Kostylev, M. P., Serga, A. A., Schneider, T., Leven, B. & Hillebrands, B. *Applied Physics Letters* **87**, 153501 (2005).
6. Schneider, T. *et al. Applied Physics Letters* **92**, 022505 (2008).
7. Lee, K.-S. & Kim, S.-K. *Journal of Applied Physics* **104**, 053909 (2008).
8. Khitun, A. & Wang, K. L. *Superlattices and Microstructures* **38**, 184 (2005).
9. Khitun, A. *et al. MRS Online Proceedings Library* **1067**, B01 (2008).
10. Khitun, A., Bao, M. & Wang, K. L. *Magnetics, IEEE Transactions on* **44**, 2141 (2008).
11. Lenk, B., Ulrichs, H., Garbs, F. & Münzenberg, M. *Physics Reports* **507**, 107 (2011).
12. Mathieu, C. *et al. Physical Review Letters* **81**, 3968 (1998).
13. Wu, H. J., Smith, C. V., Collins, J. H. & Owens, J. M. *Electronics Letters* **13**, 610 (1977).
14. Silva, T. J., Lee, C. S., Crawford, T. M. & Rogers, C. T. *Journal of Applied Physics* **85**, 7849 (1999).
15. Covington, M., Crawford, T. M. & Parker, G. J. *Physical Review Letters* **89**, 237202 (2002).

16. Bailleul, M., Olligs, D., Fermon, C. & Demokritov, S. O. *Europhysics Letters* **56**, 741 (2001).
17. Tsoi, M. *et al. Nature* **406**, 46 (2000).
18. Weber, W., Riesen, S. & Siegmann, H. C. *Science* **291**, 1015 (2001).
19. Kiselev, S. I. *et al. Nature* **425**, 380 (2003).
20. Fiebig, M. *Journal of Physics D: Applied Physics* **38**, R123 (2005).
21. Kim, S.-K., Shin, S.-C. & No, K. *Magnetics, IEEE Transactions on* **40**, 2637 (2004).
22. Lei, N. *et al. Physical Review B* **84**, 012404 (2011).
23. Bur, A. *et al. Journal of Applied Physics* **109**, 123903 (2011).
24. Bozorth, R. M. *Ferromagnetism*. (Wiley-IEEE Press: 1993).
25. Gurevich, A. G. & Melkov, G. A. *Magnetization Oscillations and Waves*. (CRC-Press: 1996).
26. Coey, J. M. D. *Magnetism and Magnetic Materials*. (Cambridge University Press: 2010).
27. Kittel, C. *Introduction to Solid State Physics*. (Wiley: 1995).
28. O'Handley, R. C. *Modern Magnetic Materials: Principles and Applications*. (Wiley-Interscience: 1999).
29. Blundell, S. *Magnetism in Condensed Matter*. (Oxford University Press, USA: 2001).
30. Herring, C. & Kittel, C. *Physical Review* **81**, 869 (1951).
31. Holstein, T. & Primakoff, H. *Physical Review* **58**, 1098 (1940).
32. Khitun, A., Bao, M. & Wang, K. L. *Superlattices and Microstructures* **47**, 464 (2010).
33. Khitun, A. & Wang, K. L. *Journal of Applied Physics* **110**, 034306 (2011).
34. Boomgaard, J., Terrell, D. R., Born, R. A. J. & Giller, H. F. J. I. *Journal of Materials Science* **9**, 1705 (1974).

35. Nan, C.-W. *Physical Review B* **50**, 6082 (1994).

36. Wang, Y., Hu, J., Lin, Y. & Nan, C.-W. *NPG Asia Materials* **2**, 61 (2010).

37. Zheng, H. *et al. Science* **303**, 661 (2004).

38. Eerenstein, W., Mathur, N. D. & Scott, J. F. *Nature* **442**, 759 (2006).

39. Manzhos, I. V. & Chupis, I. E. *Physica Status Solidi (b)* **157**, K65–K67 (1990).

40. Chupis, I. E. & Manzhos, I. V. *Ferroelectrics* **204**, 189 (1997).

41. Bichurin, M. I. *et al. Physical Review B* **64**, 094409 (2001).

42. Shastry, S., Srinivasan, G., Bichurin, M. I., Petrov, V. M. & Tatarenko, A. S. *Physical Review B* **70**, 064416 (2004).

43. Cherepov, S. *et al. Book of abstracts of the 56th Conference on Magnetism and Magnetic Materials,* DB-03, Arizona, USA (2011).

44. White, R. M. & Voltmer, F. W. *Applied Physics Letters* **7**, 314 (1965).

45. Malocha, D. C. Evolution of the SAW transducer for communication systems. *2004 IEEE Ultrasonics Symposium* **1**, 302 (2004).

46. Sreenivas, K., Sayer, M., Baar, D. J. & Nishioka, M. *Applied Physics Letters* **52**, 709 (1988).

47. Cottam, M. G. & Tilley, D. R. *Introduction to Surface and Superlattice Excitations*. (Institute of Physics Publishing Ltd., Bristol and Philadelphia: 2005)

48. Gilbert, T. L. *Magnetics, IEEE Transactions on* **40**, 3443 (2004).

49. Hillebrands, B. & Ounadjela, K. (Eds.) *Spin Dynamics in Confined Magnetic Structures I*. (Springer-Verlag, Berlin Heidelberg: 2002).

50. Skomski, R. *Simple Models of Magnetism*. (Oxford University Press, USA: 2008).

51. Donahue, M. J. & Porter, D. G. *OOMMF User's Guide, Version 1.0*. (National Institute of Standards and Technology: Gaithersburg, MD, 1999).

52. Bao, M. *et al. Applied Physics Letters* **101**, 022409 (2012).

53. Arnau, A. (Ed.) *Piezoelectric Transducers and Applications*. (Springer-Verlag, Berlin Heidelberg: 2004).

54. Wasa, K. *et al. Applied Physics Letters* **88**, 122903 (2006).

55. Soohoo, R. F. *Physical Review* **120**, 1978 (1960).

56. Rado, G. T. & Weertman, J. R. *Journal of Physics and Chemistry of Solids* **11**, 315 (1959).

57. Soohoo, R. F. *Physical Review* **131**, 594 (1963).

58. Kalinikos, B. A. & Slavin, A. N. *Journal of Physics C: Solid State Physics* **19**, 7013 (1986).

59. Kittel, C. *Physical Review* **73**, 155 (1948).

60. Griffiths, J. H. *Nature* **158**, 670 (1946).

61. Walker, L. R. *Physical Review* **105**, 390 (1957).

62. Eshbach, J. R. & Damon, R. W. *Physical Review* **118**, 1208 (1960).

63. Joseph, R. I. & Schlömann, E. *Journal of Applied Physics* **36**, 1579 (1965).

64. Demokritov, S. O., Hillebrands, B. & Slavin, A. N. *Physics Reports* **348**, 441 (2001).

65. Demokritov, S. O. (Ed.) *Spin Wave Confinement*. (Pan Stanford Publishing: 2009).

66. Jorzick, J. *et al. Physical Review Letters* **88**, 047204 (2002).

67. Park, J. P., Eames, P., Engebretson, D. M., Berezovsky, J. & Crowell, P. A. *Physical Review Letters* **89**, 277201 (2002).

68. Dvornik, M. Ph.D. thesis, University of Exeter, (2011).

69. Varadan, V. K., Suh, W. D., Xavier, P. B., Jose, K. A. & Varadan, V. V. *Smart Materials and Structures* **9**, 898 (2000).

70. Simons, R. N. *Coplanar Waveguide Circuits Components & Systems*. (Wiley-IEEE Press: 2001).

71. Zou, H., Zhang, H., Song, C., Wang, H. & Wang, P. *International Journal of Electronics* **97**, 715 (2010).

72. Vlaminck, V. & Bailleul, M. *Science* **322**, 410 (2008).

73. Shabadi, P. *et al. Nanoscale Architectures (NANOARCH), 2011 IEEE/ACM International Symposium on* 107 (2011).

74. Hillebrands, B. *Physical Review B* **41**, 530 (1990).

75. Kittel, C. *Physical Review* **110**, 836 (1958).

76. Bömmel, H. & Dransfeld, K. *Physical Review Letters* **3**, 83 (1959).

77. Schlömann, E. *Journal of Applied Physics* **31**, 1647 (1960).

78. Strauss, W. *Journal of Applied Physics* **36**, 118 (1965).

79. Wu, T. *et al. Journal of Applied Physics* **109**, 07D732 (2011).